Acta Materialia 163 (2019) 208–225

Contents lists available at ScienceDirect

Acta Materialia

journal homepage: www.elsevier.com/locate/actamat

Full length article

Semi-solid deformation of Al-Cu alloys: A quantitative comparison between real-time imaging and coupled LBM-DEM simulations

T.C. Su [a, *], C. O'Sullivan [b], T. Nagira [c], H. Yasuda [d], C.M. Gourlay [a]

[a] Department of Materials, Imperial College London, London, SW7 2AZ, UK
[b] Department of Civil and Environmental Engineering, Imperial College London, London, SW7 2AZ, UK
[c] Joining and Welding Research Institute, Osaka University, 567-0047, Japan
[d] Department of Materials Science and Engineering, Kyoto University, 606-8501, Japan

ARTICLE INFO

Article history:
Received 17 July 2018
Received in revised form
3 October 2018
Accepted 4 October 2018
Available online 9 October 2018

Keywords:
Semi-solid
Dilatancy
Synchrotron radiation
Image analysis
Discrete element method

ABSTRACT

Semi-solid alloys are deformed in a wide range of casting processes; an improved understanding and modelling capability is required to minimise defect formation and optimise productivity. Here we combine thin-sample in-situ X-ray radiography of semisolid Al-Cu alloy deformation at 40–70% solid with 2D coupled lattice Boltzmann method - discrete element method (LBM-DEM) simulations. The simulations quantitatively capture the key features of the in-situ experiments, including (i) the local contraction and dilation of the grain assembly during shear deformation; (ii) the heterogeneous strain fields and localisation features; (iii) increases in local liquid pressure in regions where liquid was expelled from the free surface in the experiment; and (iv) decreases in liquid pressure in regions where surface menisci are sucked-in in experiments. The verified DEM simulations provide new insights into the role of initial solid fraction on the stress-deformation response and support the hypothesis that the behaviour of semi-solid alloys can be described using critical state soil mechanics.

1. Introduction

Pressurised casting processes such as high-pressure die-casting [1–3], squeeze casting [4,5], and twin-roll casting [6–8] are widely used in metal processing. These casting techniques often induce shear deformation with compressive stresses on semi-solid alloys containing a solid network, and the complex stress and strain localisation can lead to casting defect formation such as concentrated porosity [9–12], macrosegregation [7,13–16] and shear cracking [15]. These defects have been related to the occurrence of shear-induced dilation [9,10,16–19], and subsequent strain localisation. The behaviour is similar to the Reynolds' dilatancy phenomenon [20] in densely packed granular materials [21], whose load:deformation behaviour is well-described by critical state soil mechanics [22]. In the last decade, in-situ deformation experiments on semi-solid alloys using thin-sample radiography [23–30] and bulk-sample tomography [31–33] have enabled direct observation of semi-solid deformation mechanisms. These have directly confirmed that shear-induced dilation [24,34] leads to grain rearrangement and strain localisation, and can cause macrosegregation [27,34] and shear-cracking [34].

Modelling studies of semi-solid deformation have included thixotropic viscosity-based models [35–37]; strain localisation criteria [38,39]; finite-element microstructure-based models at high solid fraction [40,41]; models of deformation-induced macrosegregation (e.g. in the continuous casting of steel [42–45]); and models of hot tearing under tensile load [46–48]. In most of these cases, the models do not account for isothermal shear-induced volume changes including dilatancy. To address this, here we adopt the particulate discrete element method (DEM), as it is well-suited to modelling deformation involving grain rearrangement within a solid network with dilatancy, coupled with the lattice Boltzmann method to simulate the behaviour of the interstitial liquid; this approach has not previously been used in semi-solid metals research.

In DEM, each particle (grain) in an assembly is explicitly modelled, the force imposed at each grain-grain contact is determined by a specified force-displacement law [49], and grain displacements are determined explicitly by considering dynamic equilibrium. Particulate DEM has been broadly applied to simulate deformation in granular matter such as soils [49], rock-liquid

* Corresponding author.
E-mail address: t.su14@imperial.ac.uk (T.C. Su).

https://doi.org/10.1016/j.actamat.2018.10.006

mixtures [50,51], partially molten magma [52], cement pastes [53,54], and powder metallurgy [55,56]. Furthermore, coupling with the lattice Boltzmann method (LBM) allows the behaviour of the interstitial liquid phase to be captured and solid-liquid momentum interactions to be modelled [57–61]. A few studies have also applied DEM to simulate semi-solid alloy deformation [62–64]; Sistaninia et al. [62,63] developed a 3D model for high solid fraction deformation based on a combined discrete/finite element method, while Yuan et al. [64] simulated dendrite rearrangement and shear-induced dilation behaviour as a function of solid fraction during 2D equiaxed dendritic solidification. However, these studies did not apply a coupled DEM-LBM approach to account for the particle-liquid interactions.

In this paper, we begin by analyzing four synchrotron radiography datasets of shear deformation in globular semi-solid alloys at 44–71 vol % solid, each containing ~1000–2000 grains in the field of view and approximately one grain thick. The relatively large grain assemblies enable a study of the development of strain heterogeneities and localisation features. The synchrotron datasets are quantified by X-ray intensity analysis and digital image correlation (DIC). A 2D liquid-solid coupled LBM-DEM model is then developed using the initial microstructures from the synchrotron experiments as inputs. A single set of DEM parameters was determined by calibrating the model across all deformation experiments from 44 to 71% solid so that only the initial solid fraction and contact stress were varied in the parametric study. The simulations and experiments are compared quantitatively, and then the simulations are used to extract deeper insights into the semi-solid deformation mechanisms occurring in the experiments.

2. Methods

2.1. Synchrotron radiography

Al-Cu alloys containing 8 and 15 wt% Cu and grain refined with 1 wt% Al-5Ti-–1B were cast into a steel mould to create fine equiaxed dendritic microstructures. Slices with thickness 150–200 μm were prepared from the casting. A slice of alloy was placed in the 200 μm thick cavity between two Al_2O_3 windows, and two BN plates were attached to complete the specimen cell as described in Ref. [26].

In-situ experiments were conducted on beamline 20B2 at the SPring-8 synchrotron using in-situ heating and recording apparatus described previously [26,65]. A 16 keV X-ray beam was used. Signals were recorded at 1 frame per second in 2048 × 2048 pixel format with 16-bit depth. In each experiment, the whole deformation system was heated in the furnace to a temperature in the solid + liquid region, and a semi-solid alloy with globular morphology was attained by isothermally holding the equiaxed microstructure for 30 min. Isothermal shear deformation was then applied by the upward displacement of a mobile Al_2O_3 push plate at 30 $\mu m\,s^{-1}$. Experiments were performed on samples containing 44%, 50%, 66%, and 71% solid. The experimental parameters are listed in Table 1.

2.2. Synchrotron image processing and quantification

In order to calculate the initial volumetric solid fraction, g_S^0, X-ray intensity processing was applied to the radiographs. For an isothermal mush with fully mixed liquid, in each transmitted image the intensity at a pixel, I_{SL}, is mainly a function of the solid fraction in that beam path, the X-ray absorption coefficients, and the sample thickness [23,66]:

$$I_{SL} = I_0 e^{-(\mu_{cell}L_{cell})} e^{-\mu_L\left(L_{alloy}-L_S\right)} e^{-\mu_S L_S} \tag{1}$$

where I_0 is the incident X-ray intensity, μ_L, μ_S, and μ_{cell} are the X-ray absorption coefficients of the liquid, solid and shear cell (i.e., Al_2O_3 windows). L_{alloy}, L_S are the length of semi-solid alloy and solid in the beam path respectively. As the deformation experiments were conducted isothermally, the X-ray absorption coefficients can be regarded as constants. For the initial radiograph I_{SL}^0 (^{0} indicates parameters prior to deformation), it is assumed that the sample thickness L_{alloy}^0 was uniform, so the intensity of the transmitted beam through the alloy I_{SL}^0 is only a function of L_S^0 and can be linked to the solid fraction $g_{S.A}^0$ in a given averaging area A [23]:

$$\frac{L_S^0}{L_{alloy}^0} = \frac{\ln I_{SL}^0 - \ln I_L^0}{\ln I_S^0 - \ln I_L^0} \tag{2a}$$

$$g_{S.A}^0 = \left\langle L_S^0 \middle/ L_{alloy}^0 \right\rangle_A \tag{2b}$$

where I_L^0 is the transmitted intensity through 100% liquid and equals to $I_{SL}^0(L_S^0 = 0)$, I_S^0 is the transmitted intensity through 100% solid and equals to $I_{SL}^0(L_S^0 = L_{alloy}^0)$, and A is the averaging area on L_S^0/L_{alloy}^0 to derive solid fraction, $g_{S.A}^0$. The I_L^0 and I_S^0 fields were evaluated from the local intensity minimum/maximum images $I_{SL.min}^0$, $I_{SL.max}^0$ using a rolling-ball algorithm [67] on the radiograph I_{SL}^0 prior to deformation. Throughout the paper, the average stress and strain measurements were determined by using a consistent normalised REV size to account for the effect of grain size on the quantification of stress and strain heterogeneity. In all cases the REV size was normalised by the grain size of the corresponding experiment/simulation. The rolling-ball radius was the nearest integer of $\sqrt{10}\bar{d}/2$ ($\bar{d}$ is the mean grain size measured by a line intercept method) in order to obtain representative minimum and maximum intensities. The $I_{SL.min}^0$ and $I_{SL.max}^0$ can be simply rewritten as $I_{SL}^0(L_S^0 = L_{S.min}^0)$ and $I_{SL}^0(L_S^0 = L_{S.max}^0)$ where $L_{S.min}^0$ and $L_{S.max}^0$ are the local minimum and maximum thickness of solid phase defined from rolling-ball scanning, respectively. To relate the $I_{SL.min}^0$ and $I_{SL.max}^0$ fields to the I_L^0 and I_S^0 fields, two multipliers r_L and r_S were introduced to let $r_L \cdot I_{SL.min}^0$ converge to the centre of liquid interstices, and let $r_S \cdot I_{SL.max}^0$ capture the brightest pixel of grains. The volume fraction of solid, g_S^0, was then obtained by averaging L_S^0/L_{alloy}^0 values within the FOV, which can be represented as $g_S^0 = g_{S.FOV}^0 = \left\langle L_S^0/L_{alloy}^0 \right\rangle_{FOV}$ with the assumption of $I_L^0 = r_L \cdot I_{SL.min}^0$ and $I_S^0 = r_S \cdot I_{SL.max}^0$. With this approach, the measured initial volume fraction of solid was 44%, 50%, 66%, and 71% for these four samples.

The initial volumetric solid fraction, g_S^0, coupled with the bulk alloy compositions were applied to calculate the X-ray absorption coefficient of the liquid, μ_L, and solid, μ_S [68]:

$$\mu_L = \bar{\rho}_L \left[\left(\frac{\mu}{\rho}\right)_{Al} w_{Al,L} + \left(\frac{\mu}{\rho}\right)_{Cu} w_{Cu,L} \right] \tag{3a}$$

$$\mu_S = \bar{\rho}_S \left[\left(\frac{\mu}{\rho}\right)_{Al} w_{Al,S} + \left(\frac{\mu}{\rho}\right)_{Cu} w_{Cu,S} \right] \tag{3b}$$

where $\bar{\rho}_L$ and $\bar{\rho}_S$ are liquid and solid densities calculated using reference [69], $w_{Al,L}$, $w_{Cu,L}$, $w_{Al,S}$, and $w_{Cu,S}$ are the mass fractions of aluminium and copper in the liquid (L) and solid (S) from the phase

Table 1
A summary for in-situ observation on semi-solid deformation experiments performed at the SPring-8 synchrotron facility, Hyogo, Japan. The push-plate moving rate was measured directly from time-series images. The average semi-solid alloy grain size was measured by applying the line interception method on the initial radiographic projection image (ASTM E112-96 standard test method). The volume fraction of solid was evaluated by applying a volume averaging method to the initial image (see Supplementary Information 1).

Parameters (experiment#)	Unit	44% solid (15071202)	50% solid (15071409)	66% solid (15071203)	71% solid (18013006)
Alloy composition	wt.%	Al-15Cu-0.05Ti-0.01B	Al-15Cu-0.05Ti-0.01B	Al-8Cu-0.05Ti-0.01B	Al-8Cu-0.05Ti-0.01B
Average grain size, $\bar{d}$	μm	80	120	130	120
Average volume fraction of solid, g_s^0	–	44%	50%	66%	71%
Sample dimension width × height	mm	10.0 × 5.0	10.0 × 10.0	7.5 × 10.0	10.0 × 10.0
Radiography pixel size	μm	2.5	2.5	2.5	2.75
Field of view (FOV)	mm	5.1 × 5.1	5.1 × 5.1	5.1 × 5.1	5.6 × 5.6
Averaging size for local solid fraction, A	pxl	101	151	165	139
X-ray absorption coefficient of liquid, μ_L	cm^{-1}	59.6	63.3	49.1	52.6
X-ray absorption coefficient of solid, μ_S	cm^{-1}	22.9	23.5	21.3	21.8

diagram [70], and $(\mu/\rho)_{Al}$, $(\mu/\rho)_{Cu}$ are the mass X-ray absorption coefficients of pure aluminium and copper at 16 keV X-ray energy [71]. The evaluated μ_L and μ_S were used to calculate L^0_{alloy} and $L^0_{S.min}$ prior to deformation:

$$L^0_{alloy} = \left\langle \frac{\ln I^0_S - \ln I^0_L}{\mu_L - \mu_S} \right\rangle_{FOV} \tag{4a}$$

$$L^0_{S.min} = \left\langle \frac{\ln I^0_{SL.min} - \ln I^0_L}{\mu_L - \mu_S} \right\rangle_{FOV} \tag{4b}$$

With this approach, the initial thickness of the semi-solid was calculated to be 180 ± 30 μm for the four samples, consistent with expectation.

The solid fraction field, $g^0_{S.REV}$, was obtained for images before and during deformation by volume averaging L^0_S/L^0_{alloy} over projected areas of $\sqrt{10\bar{d}} \times \sqrt{10\bar{d}}$ which is a representative elementary volume (REV) that is sufficiently large to average the local microstructure and small enough that important variations in the solid fraction $g^0_{S.REV}$ can be captured [72,73]. The averaging REV size and X-ray absorption coefficients are summarised in Table 1. A detailed example of finding the g^0_S and $g^0_{S.REV}$ fields from radiographs is illustrated in Supplementary Information (SI) Section 1.

During deformation, the local sample thickness can change. The sample thickness field in frame n, L^n_{alloy} can be found through rearranging Eq. (1) and obtaining $I^n_{SL.min}$ by applying the rolling-ball algorithm on each radiograph I^n_{SL}:

$$L^n_{alloy} = L^0_{alloy} + \frac{\ln\left(I^0_{SL.min}/I^n_{SL.min}\right)}{\mu_L} + \frac{(\mu_L - \mu_S)\left(L^n_{S.min} - L^0_{S.min}\right)}{\mu_L} \tag{5}$$

where $L^n_{S.min}$ is the local minimum thickness of solid phase. Alternatively, L^n_{alloy} can be evaluated from the transmitted intensity through a point of 100% solid in frame n, I^n_S through rearranging Eq. (1):

$$L^n_{alloy} = \frac{\ln I^0_S - \ln I^n_S}{\mu_S} + L^0_{alloy} \tag{6}$$

Whether Eq. (5) or Eq. (6) is better suited to calculating L^n_{alloy} depends on whether $L^n_{S.min}$ or I^n_S can be more accurately measured. To proceed, we identified regions that meet one of the following three criteria.

- For regions with sufficiently small deformation, the change of $L^n_{S.min}$ can be neglected. Therefore, it was assumed that for any REV with an average grain displacement $< 0.05u^n_y$, $L^n_{S.min} = L^0_{S.min}$ in Eq. (5). (u^n_y is the y-component of push-plate displacement in frame n):
- For regions with a sufficiently large liquid interstice, the $I^n_{SL.min}$ can be regarded as the intensity of liquid, I^n_L. Therefore, it was assumed that for any REV with a liquid interstice $\geq 0.2\bar{d} \times 0.2\bar{d}$, $L^n_{S.min} = 0$ in Eq. (5).
- For regions with highly-compacted solid grains (i.e., in front of the push plate), the $I^n_{SL.max}$ can be regarded as the intensity of the solid, I^n_S. Therefore, it was assumed that for any REV with average grain displacement $> 0.95u^n_y$ and $u^n_y > 0.25$ mm, the $I^n_S = I^n_{SL.max}$ and L^n_{alloy} was found using Eq. (6).

Sufficient regions met one of these three criteria that the whole L^n_{alloy} field could be computed from interpolation of ≈100 scattered $L^n_{alloy}(x, y)$ points per frame. A step-by-step guide to the procedure is given in SI Section 2. The volumetric solid fraction field for radiograph n, $g^n_{S.REV}$, was then obtained:

$$I^n_L = I^0_L e^{-\mu_L\left(L^n_{alloy} - L^0_{alloy}\right)} \tag{7}$$

$$g^n_{S.REV} = \left\langle \frac{L^n_S}{L^n_{alloy}} \right\rangle_{REV} = \left\langle \frac{\ln I^n_{SL} - \ln I^n_L}{L^n_{alloy}(\mu_L - \mu_S)} \right\rangle_{REV} \tag{8}$$

The volumetric strain of any representative element, ε^n_{vol}, was evaluated from the volume-averaged solid fraction $g^0_{S.REV}$ and $g^n_{S.REV}$ using Eq. (9) which is derived in SI Section 2:

$$\varepsilon^n_{vol} = \frac{g^0_{S.REV}}{g^n_{S.REV}} - 1 \tag{9}$$

2.3. Digital image correlation (DIC) analysis

DIC analysis was applied on the synchrotron datasets using the 2D Strain Module in DaVis 8.3 software (LaVision Imaging Company, Göettingen, Germany). The side length of the square subset used for correlation was the nearest odd integer of $\sqrt{10\bar{d}_{pxl}}$ ($\bar{d}_{pxl}$ is the mean grain size in pixels) similar to the REV for deriving $g_{S.REV}$ in order to offer sufficient greyscale pattern for correlation while mapping heterogeneous strain. The step size was set to the nearest integer of $\sqrt{10\bar{d}_{pxl}}/4$ to reconstruct the displacement vector field with reasonable resolution. The DIC parameters used are listed in Table 2. The accumulated displacement was conducted by

Table 2
Summary of parameters selected for conducting digital image correlation (DIC).

Parameters	Unit	44% solid	50% solid	66% solid	71% solid
Average grain size, $\overline{d}$	μm	80	120	130	120
Average grain size, $\overline{d}$ in pixels	pixel	32	48	52	44
Correlation subset size	pixel	101	151	165	139
Correlation step size	pixel	25	38	41	35

summing all displacement vectors from the correlation between the 1st/2nd frames to (n-1)th/nth frames for each calculation point. The conversion to rotation-free strain fields was performed by partial differentiation on the accumulated displacement vector field and using the polar decomposition algorithm [74]. Finally, all of the displacement vector fields and strain fields were filtered by the bilinear interpolation method [75,76] to smooth out discontinuous features.

2.4. Discrete element method (DEM) simulations

Since DEM is not commonly used in semi-solid alloy modelling, the general principles are outlined here. DEM is a dynamic modelling technique that idealises an assembly of solid particles as quasi-rigid bodies in mechanical contact. Initial and boundary conditions are specified and the main calculations take place at discrete time intervals; these calculations determine the forces and moments acting on each particle/grain, and update the particle positions and orientations. The force and moment (scalar in 2D DEM) components considered here arise from Ref. [49]:

1. Pair-wise contact: direct interaction between two grains, or between a grain and wall. These are determined via a contact detection phase that identifies contacting particles and using contact models that relate grain overlap to a contact force.
2. Pair-wise bonding: non-contact bonding that allows tensile contact forces between grains (this is used to simulate the membrane boundary here)
3. Gravitational (body) force. The DEM model used here does not include a gravitational field since the movement of grains in the experiment is observed to be majorly controlled by the physical contact between grain surfaces rather than gravity.

   In each DEM calculation cycle, the dynamic equilibrium of each particle is considered to determine an acceleration, a Verlet-type explicit time integration is then used to determine the particle displacements and rotations for the current time step from the acceleration value. The particle positions, orientations and velocities are updated and these new positions and velocities are used to calculate the contact and drag forces for the next time increment. DEM is algorithmically similar to molecular dynamics.
4. Drag force and moment from liquid flow.

Digital 2D grain assemblies were generated to represent each microstructure from the thin sample (~1 grain thick) experiments. To obtain the size and shape distributions, 120 grains were picked from a radiograph prior to deformation for each dataset (Fig. 1a and b). The perimeter of each grain was identified using the “point picker” plugin in ImageJ (National Institute of Health, USA), and a least-squares elliptical function was fitted to the perimeter points, as shown in Fig. 1c. The usage of the elliptical function was because this gave a good fit to the actual globular grain shape while capturing the asphericity in a computationally efficient way. To reduce the calculation cost further, each ellipse was simplified as two equivalent overlapping circles (Fig. 1d). Grain size and shape distributions were reproduced by picking and simplifying 120 grains from the radiograph and converting them into 20 grain templates to generate a grain assembly in the DEM package PFC2D Ver. 5.0 (Itasca Consulting Group, Inc). To generate a DEM sample, these grains with normal stiffness 1×10^4 N/m were constrained by a rectangular box with the same size as the thin-plate sample for each experiment, and then isotropic compression was applied by a servo-controlled mechanism until a target 2D stress of 500 N/m was reached.

Examination of experimental radiographs showed that the outside Al_2O_3 wall did not touch the semi-solid samples as shown in SI Section 3 (Fig. SI-6) except for the left edge of the 71% solid sample and there was only a small degree of surface deformation (with displacement $< 0.15\overline{d}$). We can infer from this that the sample is constrained by surface tension, i.e. the motion of a grain at the free surface would increase the local curvature of the liquid-air interface, which would decrease the local liquid pressure and apply a suction that resists grain motion. In this way, the surface grains have an apparent cohesion and surface tension stabilises the free surfaces against gravity and prevents slumping. To simulate the apparent cohesion, the rigid walls were deleted and the surface grains were assigned partial cohesion using parallel bonds in PFC2D that create a movable membrane boundary that constrains the packing of grains similar to reference [77,78]. These parallel-bonded surface grains are shaded red and linked by red lines in Fig. 1e–g. With this approach, a constraint force, $\mathbf{F_N}$, would be installed on any membrane grain if the grain started to displace outward, and the direction of $\mathbf{F_N}$ for the membrane circle was determined from the position of its two adjacent membrane grains (Fig. 1h and i). The sample generation stage finished when the maximum magnitude of grain velocity in the system was less than 10^{-7} m/s, and the average contact force magnitude excluding membrane circles, F_0, was extracted to obtain the extent of the pre-existing force network for each sample. The initial 2D packing fraction, $f^0_{S.pk}$, was measured for each assembly by randomly distributing 5000 measurement circles with diameter $2\overline{d}$ across the whole assembly (see SI Section 7 for the descriptions of measurement circle). To simulate the push-plate, a new rigid wall was introduced as illustrated in Fig. 1e. The use of measurement circles as a representative volume (RV) follows measurement approaches in the DEM literature [79–81]. The concept of a circular RV in DEM analysis here is different from the use of square/rectangular REVs for image analysis suggested by Ref. [23].

The key parameters used for the DEM simulations are summarised in Table 3. The solid phase densities differed in the four virtual samples because experiments were either carried out at different temperatures or with different bulk alloy compositions to achieve the range of solid fractions, and the density was calculated using the composition and temperature-dependent equations of ref. [69]. However, the simulated results would not be significantly altered if a single density had been used across all simulations. A low sliding friction coefficient, μ, was used at contacts as the liquid phase is expected to provide lubrication, while the rolling-

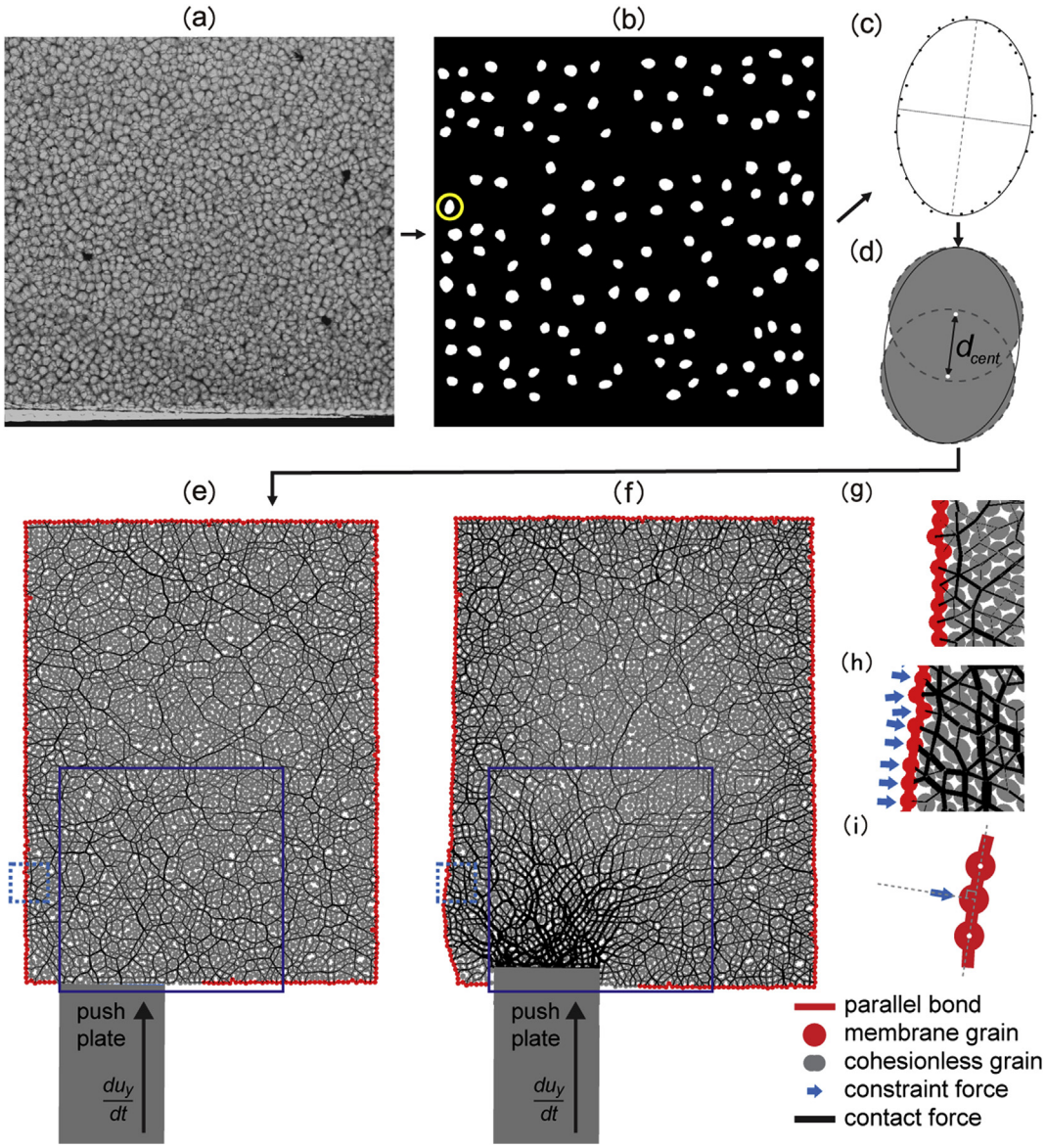

Fig. 1. The procedure to simulate semi-solid deformation adapting microstructures from deformation experiments: (a) in-situ synchrotron radiography imaging on 66% solid sample before deformation, (b) 120 particles selected for shape analysis, (c) circled particle in (b) fitted using an elliptical equation, and (d) the corresponding two-circle grain used to represent the shape of the fitted ellipse in (c). After adapting particle size and shape distribution by measuring 120 particles, a grain assembly (simulation C) was created which was constrained by the push plate and membrane as shown in (e), and (f) is the deformation microstructure during push-plate displacement with rate $du_y/dt = 30\ \mu m\ s^{-1}$. The black lines in (f) indicate the contact force chain and the thickness of each line is proportional to the contact force magnitude. The blue solid square in (e–f) indicates the corresponding field of view in X-ray imaging. (g–h) The cropped region from the dash-line square in (e) and (f), respectively. (h) Showing that constraint force normal to the membrane was applied as the membrane boundary deformed, and (i) the determination of normal force direction from two adjacent circles. (For interpretation of the references to colour in this figure legend, the reader is referred to the Web version of this article.)

resistance coefficient, μ_r, was specified from the consideration of the non-spherical shape of particles and the existence of contact surfaces rather than point contacts [82]. High bonding strengths were assigned to the membrane contacts to prevent bond breakage.

Past DEM studies have shown that, provided changes in the mean grain size do not significantly alter the number of grains in the sample, many of the deformation features scale with the mean grain size [83,84]. The contraction or dilation behaviour is sensitive to initial solid fraction and the average grain size plays a more minor role, mainly affecting the magnitude of volume change.

To account for the plastic deformation of grains during shear deformation, the contact force-overlap relationship in Fig. 2a was applied. This represents the flow curve of Al alloys deformed at constant shear rate without work hardening after yielding (U_y, F_y) at homologous temperature near to 1.0 [85]. The setting of an elastic unloading/reloading path between an unloading point (U_{un}, F_{un}) and residual overlap point $(U_{res}, 0)$ shown in Fig. 2a enables the grain-grain contact to follow the behaviour of cyclic loading in alloys [86]. This plastic force-overlap relationship did not apply on the grain-wall contacts or any bonded contacts between two circular membrane grains. The membrane boundary and plastic force-overlap relationship were incorporated using the embedded scripting language *FISH* in PFC2D, and the detailed code descriptions are in SI Section 4.

Table 3
Parameters used during shear deformation stage. The initial void ratio $e_0 = (1 - f^0_{S.pk})/f^0_{S.pk}$.

Property	Unit	Value
Grain density, ρ	kg m^{-3}	
Simulation A, for 44% solid sample		2643
Simulation B, for 50% solid sample		2658
Simulation C, for 66% solid sample		2620
Simulation D, for 71% solid sample		2625
Elastic normal stiffness, $k_{n.e}$	N m^{-1}	4×10^{-3}
Slope of plastic flow regime[a], $k_{n.p}$	N m^{-1}	1×10^{-7}
Grain-wall normal stiffness, $k_{n.g-w}$	N m^{-1}	6×10^{-3}
Membrane circle normal stiffness, $k_{n.mem}$	N m^{-1}	0.013
Membrane bonding normal stiffness, $k_{n.bond}$	N m^{-2}	13
Tensile strength of bonding, σ_{bond}	N m^{-1}	2×10^{10}
Shear strength of bonding, τ_{bond}	N m^{-1}	1×10^{10}
Membrane bonding radius multiplier, $\overline{\lambda}_{bond}$	–	0.5
Normal-to-shear stiffness ratio, κ	–	2.0
Average contact force magnitude prior to def., F_0	N	
Simulation A, for 44% solid sample		0
Simulation B, for 50% solid sample		2.52×10^{-9}
Simulation C, for 66% solid sample		1.64×10^{-8}
Simulation D, for 71% solid sample		3.24×10^{-8}
Initial 2D packing fraction:void ratio, $f^0_{S.pk}$:e_0	–	
Simulation A, for 44% solid sample		0.78:0.28
Simulation B, for 50% solid sample		0.81:0.23
Simulation C, for 66% solid sample		0.89:0.12
Simulation D, for 71% solid sample		0.92:0.09
Total number of grains, N^{DEM}_{grain}	–	
Simulation A, for 44% solid sample		7907
Simulation B, for 50% solid sample		7054
Simulation C, for 66% solid sample		5224
Simulation D, for 71% solid sample		8328
Minimum:maximum grain size, d^{DEM}_{min}:d^{DEM}_{max}	μm	
Simulation A, for 44% solid sample		64:105
Simulation B, for 50% solid sample		91:165
Simulation C, for 66% solid sample		110:164
Simulation D, for 71% solid sample		90:160
Effective mean overlap prior to deformation, U_0	m	$F_0/k_{n.e}$
Yielding contact overlap, U_y	m	U_0+4.0 × 10^{-7}
Yielding force, F_y	N	$k_{n.e} \cdot U_y$
Normal force on membrane, F_N	N	$0.25 \cdot F_y$
Friction coefficient, μ	–	0.05
Rolling friction coefficient, μ_r	–	0.5
Simulation timestep[b], Δt	s	6.66×10^{-6}

[a] To ensure the mechanical stability of deformation simulation, there is a nonzero slope of force-overlap relationship after yielding point corresponding to the red line in Fig. 2a.

[b] The timestep setting allows the push plate have a constant vertical displacement 2.00×10^{-10} m between two calculation cycles for all simulation datasets.

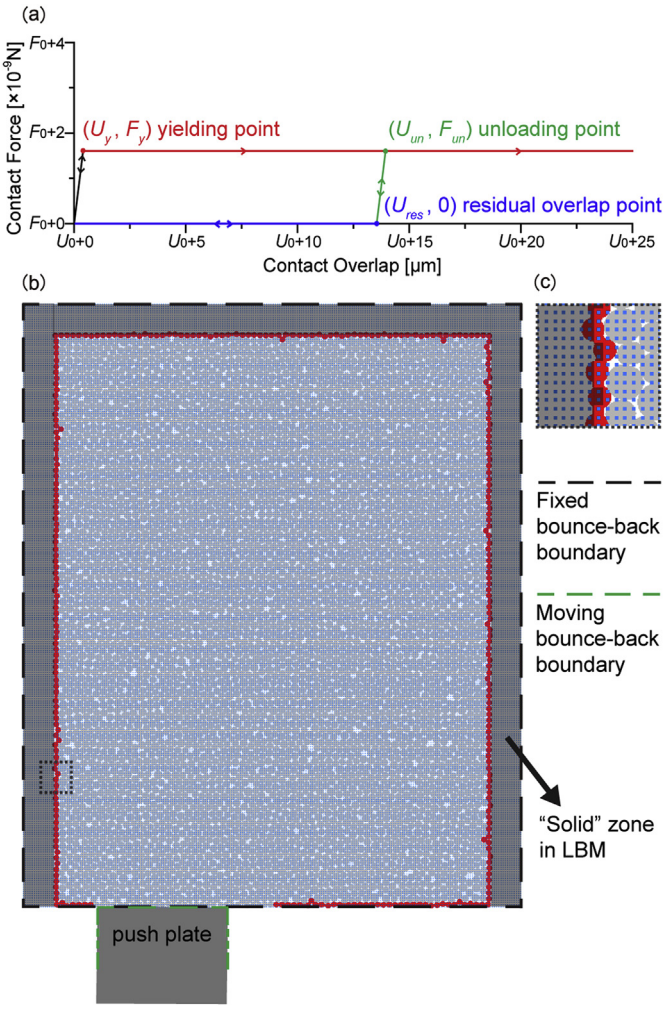

Fig. 2. (a) Normal force-overlap relationship used in the DEM simulation where F_0 is the mean contact force prior to deformation related to initial solid fraction g^0_S, and U_0 is the corresponding mean contact overlap. (b) Installing the Al-Cu liquid domain on the DEM grain assembly (Fig. 1e) by setting liquid lattice nodes and liquid boundary conditions. The Al-Cu liquid domain is controlled by fixed bounce-back boundary (black dashed line), moving bounce-back boundary (green dashed line), and solid zone outside of the membrane (grey-shaded area) corresponding to the lattice solid fraction $\varepsilon = 0$. (c) The magnified view of the dashed grey box in (b) showing the DEM grains, membrane circles, solid zone, and lattice nodes with spacing 40μm. (For interpretation of the references to colour in this figure legend, the reader is referred to the Web version of this article.)

2.5. LBM-DEM two-phase coupling

In order to incorporate the liquid phase, the lattice Boltzmann method (LBM) was applied and LBM-DEM coupling as proposed by Cook et al. [57] was used. The LBM solves the Navier-Stokes equations for the liquid on a regular grid. Each grid node contains a packet of liquid particles that are allowed to move in horizontal, vertical and diagonal directions. The grid nodes in the vicinity of a liquid-solid surface act as a no-slip bounce-back boundary to the interstitial liquid. The detailed description of governing equations and key parameters in the LBM-DEM coupling adopted in this research is given in SI Section 5.

The rectangular LBM grid extended beyond the DEM sample boundaries (Fig. 2b). The lattice spacing was 40 μm, and the average grain size $\overline{d}$ to lattice spacing ratios were 2–3; an immersed boundary scheme was used to achieve sub-lattice resolution. The liquid density, ρ_L, calculated from Ref. [69], dynamic viscosity, μ_L, from Ref. [87], and LB liquid calculation timestep are listed in Table 4. The kinematic viscosities (μ_L/ρ_L) used in the four simulations were in the narrow range 6.10–6.75 × 10^{-7} m^2/s, showing that the Cu concentration in the liquid has a minor effect on the liquid flow behaviour. Following past work on interstitial liquid flow and permeability in 2D simulations of packed granular materials and porous media [88–90], the concept of a "hydrodynamic radius" was used and set to be 0.8. This enables the liquid and solid phases to both exist as percolating networks as in the thin sample experiments. Before deformation, the liquid velocity was initialised as zero. The LB bounce-back boundary condition [91] was applied on boundary nodes (dashed black line in Fig. 2b), and the LB nodes outside of the DEM membrane boundary were identified as an effective "solid zone" to inhibit liquid Al from flowing out of the DEM sample. The solid zone applied in the LBM simulations has no effect on the DEM simulation of the grains. When the membrane deforms, the LBM solid zone adapts to the new shape of the membrane.

Table 4
Liquid parameters used in LBM-DEM coupling simulation.

Property	Unit	Value
Liquid density, ρ_L	kg m^{-3}	
Simulation A, for 44% solid sample		2903
Simulation B, for 50% solid sample		2948
Simulation C, for 66% solid sample		2787
Simulation D, for 71% solid sample		2810
Liquid dynamic viscosity, μ	Pa s	
Simulation A, for 44% solid sample		1.92×10^{-3}
Simulation B, for 50% solid sample		1.99×10^{-3}
Simulation C, for 66% solid sample		1.70×10^{-3}
Simulation D, for 71% solid sample		1.75×10^{-3}
LBM Simulation timestep[a], δt	s	6.66×10^{-4}

[a] The timestep setting in LBM was 100 times higher than DEM timestep listed in Table 3.

During shear deformation, the push plate acts as a moving bounce-back boundary [92] and nodes overlapping with the push plate are automatically identified as solid. The liquid pressure change Δp in response to shear deformation was derived from the change of liquid density for each LBM node, and the speed of sound c_s, in the LBM domain (detail in SI Section 5):

$$\Delta p(\mathbf{x}_i, t) = (\rho(\mathbf{x}_i, t) - \rho_0)c_s^2 \tag{10}$$

where ρ_0 is the initial liquid density listed in Table 4, and $\rho(\mathbf{x}_i, t)$ is the liquid density at position $\mathbf{x}_i$ at simulation time t. The liquid drag force and moment acting on DEM grains were updated by a cycle of the LBM-DEM coupling algorithm (see SI Section 5 for detail).

3. Results and discussion

3.1. Analysis of radiography image sequences

Fig. 3a–d shows processed in-situ X-ray images from four datasets prior to deformation. Each image shows the solid fraction in the beam path, L_S^0/L_{alloy}^0, at each pixel, calculated from the transmitted intensities using Eq. (2) and SI-Eq. (3). In this conversion, white represents solid ($L_S^0/L_{alloy}^0 = 1$) and black represents liquid ($L_S^0/L_{alloy}^0 = 0$). Pixels with L_S^0/L_{alloy}^0 value not falling in the range [0,1] are coloured red, and are mainly regions of oxide and pores. Fig. 3e–h are the L_S^n/L_{alloy}^n field after a push-plate displacement of $5\overline{d}$ for each dataset. The changes in intensity of the L_S^n/L_{alloy}^n shading indicate changes in the local solid fraction due to grain rearrangement and liquid flow.

The L_S^0/L_{alloy}^0 fields were volume averaged using a REV of $\sqrt{10\overline{d}} \times \sqrt{10\overline{d}}$ to obtain the solid fraction field prior to deformation (Fig. 3i–l) where the red pixels in Fig. 3a–d were excluded from the averaging process. Fig. 3i–l shows that the solid phase distribution before deformation is slightly segregated with a higher solid fraction nearer the top of the FOV. This is especially evident for the 44% solid dataset and is due to grain buoyancy in Al-15Cu where the density of the solid is lower than the liquid [69]. After a $5\overline{d}$ increment of push-plate displacement, Fig. 3m–p shows the development of more heterogeneous solid fraction field. In all samples, Fig. 3m–p shows accumulation/compaction of grains and expulsion of liquid (hotter colours) in front of the push plate where the local $g_{S.REV}^n$ is increased to $\approx$0.8. Additionally, for the 66% and 71% solid samples, a reduced solid fraction and increased liquid fraction (cooler colours) with $g_{S.REV}^n$ from 0.4 to 0.5 is present ahead of the compaction zone.

The local changes in solid fraction correspond to volumetric strains in the grain assembly, which are plotted as volumetric strain maps ε_{vol}^n in Fig. 3q–t using Eq. (9) on the volume-averaged solid fraction maps. It is clear from Fig. 3q–t that, for initial solid fractions of 44% and 50%, deformation is mostly contractive (blue) with only small pockets of local dilation (red) and, as the initial solid fraction increases, an increasing proportion of the sample undergoes shear-induced dilation (red) and the magnitude of local dilation increases. In Fig. 3q and r, the push-plate displacement on the low solid fraction datasets (44% and 50%) developed a compaction field with $\varepsilon_{vol}^n \approx -0.3$, while the compaction zone in 66% and 71% solid datasets is less significant (Fig. 3s and t), where ε_{vol}^n falls in the range $-0.2 \sim -0.1$. It should also be noted that the negative ε_{vol}^n regions to the right of the FOV in Fig. 3s and the right-bottom of the FOV in Fig. 3t represent local contraction corresponding to the suction of liquid away to the dilating regions elsewhere in the sample.

While there are differences between bulk 3D deformation and the current study on thin sample deformation with interactions with the confining walls, we note that the key features measured here have also been measured in bulk 3D tomographic imaging [31] and in microstructures after semi-solid deformation experiments. For example, shear-induced contraction in samples containing a loose solid network [17], shear-induced dilatation in samples containing a dense solid network [9,19], and the localisation of dilatancy [9].

The main deformation mechanisms that increase and decrease the solid fraction and cause volumetric strain in Fig. 3q–t, and the resultant heterogeneous solid fraction field in Fig. 3m–p are shown in Fig. 4 using the 66% solid sample as an example. In region A, the increase in solid fraction (contraction) can be seen to be due to grains being pushed closer together and expelling some interstitial liquid and, in this case, also due to compression of the individual grains. In region B, the decrease in solid fraction (dilation) is due to grains moving apart and liquid being drawn in interstitial. In region B, all grains are in mechanical contact with their neighbours and, therefore, the shear-induced dilation (dilatancy) is caused by grains pushing one another apart under the action of compressive and shear contact forces.

2D displacement fields were obtained by tracking the motion of grains using DIC. Fig. 5a–d shows the incremental displacement vectors for a push-plate displacement of 0 to $5\overline{d}$ for each dataset, and the background image is the time averaged radiographs from 0 to $5\overline{d}$ push-plate displacement for comparison. The vectors in Fig. 5a–d represent grain movement and show that, for the same push-plate displacement, grains are displaced deeper into the sample as the initial solid fraction increases. The displacement vector field in DIC can be directly converted to shear strain (ε_{xy}) fields as shown in Fig. 5e–h, where the background for each shear strain field is selected as the image at $5\overline{d}$ push-plate displacement. In Fig. 5e–h, it is clear that the ε_{xy} is highly localised above the top-right corner of push plate. The red region near to the parting plane in the 44% solid sample (Fig. 5e) is relatively small, while the red bands of localised shear strain form in 50% solid (Fig. 5f). A more-developed region of shear strain along the parting plane can be found in Fig. 5g and h which is wider and deeper than in Fig. 5e–f. From Fig. 5e–h, it can be seen that at the same push-plate displacement a higher solid fraction induces a larger area of shear strain (red) around the parting plane. The formation of blue regions in Fig. 5g and h is due to $\varepsilon_{xy} < 0$ development near to the left parting plane aligning with the top-left corner of push-plate (outside of the left edge of the FOV).

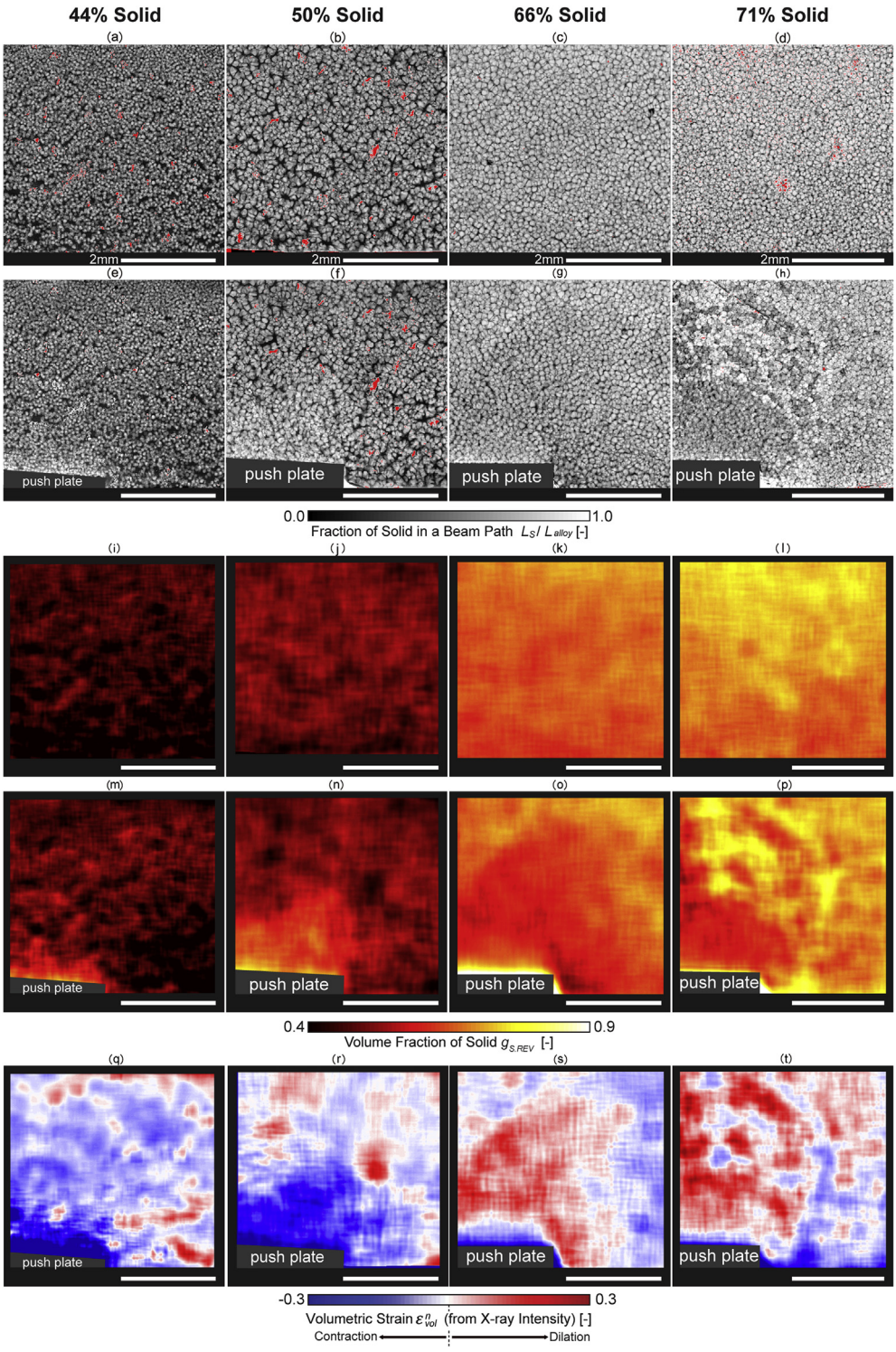

Fig. 3. Analysis of experimental X-ray datasets. (a–d) Calculation of L^0_S/L^0_{alloy} (the fraction of solid at a beam path) field on synchrotron X-ray imaging before deformation and (e–h) L^n_S/L^n_{alloy} field on deformation after $5\overline{d}$ increment of push-plate displacement. The conversion from L^0_S/L^0_{alloy} or L^n_S/L^n_{alloy} field to image is shown in SI-Eq. 3. (i–l) Average filtered results from (a–d) with window size $\sqrt{10\overline{d}} \times \sqrt{10\overline{d}}$ showing initial solid fraction field $g^0_{S,REV}$. (m–p) Average filtered results from (e–h) showing solid fraction evolution $g^n_{S,REV}$ during deformation. (q–t) The evaluation of volumetric strain ε^n_{vol} using Eq. (9). Images in the leftmost column correspond to the 44% solid sample, followed by 50%, 66%, and 71% solid samples, respectively. White-line scale bars read 2mm.

3.2. Numerical simulation results and comparative study

It was found that a single set of optimised LBM-DEM parameters could reasonably reproduce the displacement and strain fields in all four experiments while varying few parameters: the initial packing fraction (i.e. the solid fraction), the initial average contact stress, solid/liquid densities, and liquid viscosity directly linking to corresponding experiments. Note that, while the solid/liquid densities

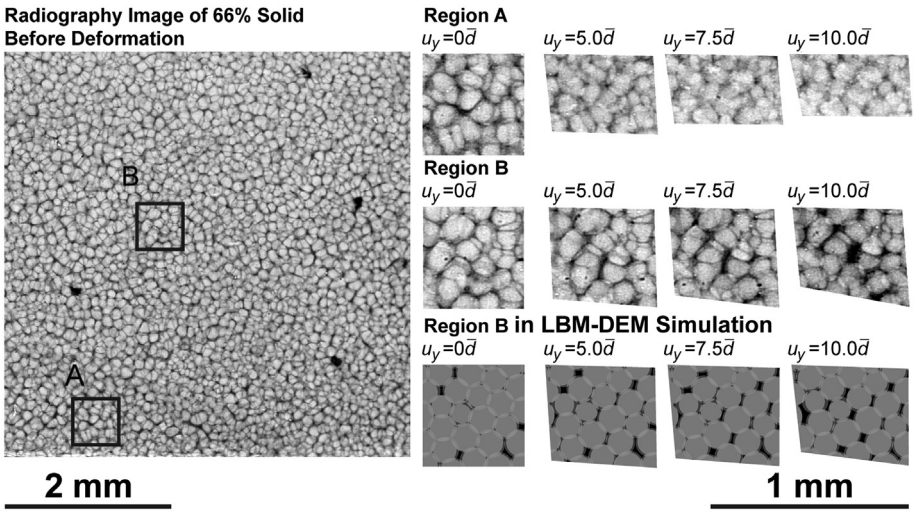

Fig. 4. Microstructure of deformation experiment at 66% solid. Two regions from the image were selected for detailed observation in order to gain insights on strain localisation. Region A shows high compaction along the y-direction, while the shear-induced dilation phenomenon can be clearly seen in region B when push-plate displacement (u_y) equals to $10\bar{d}$. Similar dilation behaviour can be observed in region B in the LBM-DEM simulation.

and liquid viscosity were calculated for the relevant temperature and phase compositions, the variation in these parameters is small and the simulated results would not be significantly altered if a single density and liquid viscosity value had been used across all simulations. Thus, effectively two parameters were varied. The optimised set of parameters including contact stiffness values and friction coefficients is shown in Table 3, and was found by an iterative approach to reproduce the deformation microstructure in each experiment across the full range of applied displacements. This was done by starting with literature values for stiffness [64,93] and friction coefficient [64,82,93,94], and then varying these to obtain a good correlation (e_{norm} in Eq. (11) within 10%) of the 1D displacement profile between simulation and experiment.

To enable direct comparison DIC analysis was performed on DEM simulated data, using the same DIC techniques and parameters as in the experimental analysis. To do this, DEM grains were coloured by random greyscale to construct a speckle pattern, the pixel size and FOV of DEM microstructure plots were adjusted to be the same as in radiography images, and the same DIC parameters were used (Table 2). Fig. 5i–l shows the result for the displacement fields, and a good correlation of vector fields between experiment (Fig. 5a–d) and simulation (Fig. 5i–l) can be seen. It can also be seen that the DIC shear strain fields from the simulations (Fig. 5m–p) correctly capture many of the shear strain localisation characteristics in the experiments (Fig. 5e–h). For example, the shape and extent of the red localised shear zones, and the influence of initial solid fraction on the shear strain fields are well reproduced. Also note from Fig. 5g and h, that the shear strain is positive just in front of the push plate for the 66% solid sample while it is negative for the 71% solid sample. This is because the boundary conditions are slightly different for these samples. In the 66% solid sample (Fig. 5g), the sample sides did not touch the Al_2O_3 side walls and, in the 71% solid sample, the left edge of the sample is in contact with the Al_2O_3 side wall (as introduced in section 2.4). The simulations in Fig. 5o and p used the boundary conditions measured for each experiment and gave a similar result. This is because constraint from the left side wall prevents grain displacement to the left, resulting in a change in shear strain direction.

The displacement vector fields in Fig. 5i–l were then interpolated and scanned to construct grain displacement profiles as shown in Fig. 6a, which plots the grain displacement relative to the push-plate displacement at various distances ahead of the push-plate along a 1D line starting at the middle of the push-plate as indicated by the vertical dashed line in Fig. 5m. Comparison of the 1D displacement profiles between experiments and simulations after a $5\bar{d}$ increment of push-plate displacement confirms that the simulation reproduces the gradient of the displacement as well as the higher relative displacement in higher solid fraction datasets. To quantify this, Fig. 6b is a bar chart of the normalised error of simulated displacement profiles compared with the experiments, e_{norm}, with increments of push-plate displacement from $1\bar{d}$ to $5\bar{d}$. The normalised error is defined as:

$$e_{\text{norm}} = \frac{1}{Y_2 - Y_1} \sum_{Y=Y_1}^{Y_2} \left| \frac{\delta^{\text{EXP}}(Y)}{u_y^{\text{EXP}}} - \frac{\delta^{\text{DEM}}(Y)}{u_y^{\text{DEM}}} \right| \times 100\% \qquad (11)$$

where $Y_1 = 250\mu\text{m}$ and $Y_2 = 3000\mu\text{m}$ are the nearest and farthest points from the middle point of the push plate in the FOV, u_y^{EXP} and u_y^{DEM} are the push-plate displacement lengths, and $\delta^{\text{EXP}}(Y)$ and $\delta^{\text{DEM}}(Y)$ are the interpolated displacement magnitude in scan point Y in an experiment and simulation. The scan resolution is 1 μm. From Fig. 6b, it can be seen that the error value e_{norm} is <10% for all experiment/simulation pairs, indicating good agreement between simulation and experiment.

We next examine how closely the simulations can reproduce the heterogeneous strain patterns observed in the radiography datasets. Comparison between localised strains can be simplified by the conversion from two-dimensional strain fields to averaged one-dimensional line profiles by averaging along x or y within a ROI, as shown from Fig. 7 to Fig. 10. In (c) and (d) of Figs. 7–10, the red lines correspond to LBM-DEM simulations and the black lines correspond to experimental measurements taken from the red ROI (box outlined by the red-dashed line in (a) and (b) of Figs. 7–10, which is averaged along y). The red ROI was selected to investigate the development of strain heterogeneity across the parting plane. In (e) and (f) of Figs. 7–10, the blue lines correspond to LBM-DEM simulations and the black lines correspond to experimental measurements taken from the blue ROI ahead of the push plate (box outlined by blue-dashed line in (a) and (b) of Figs. 7–10, which is averaged along x). The blue ROI was selected to investigate the

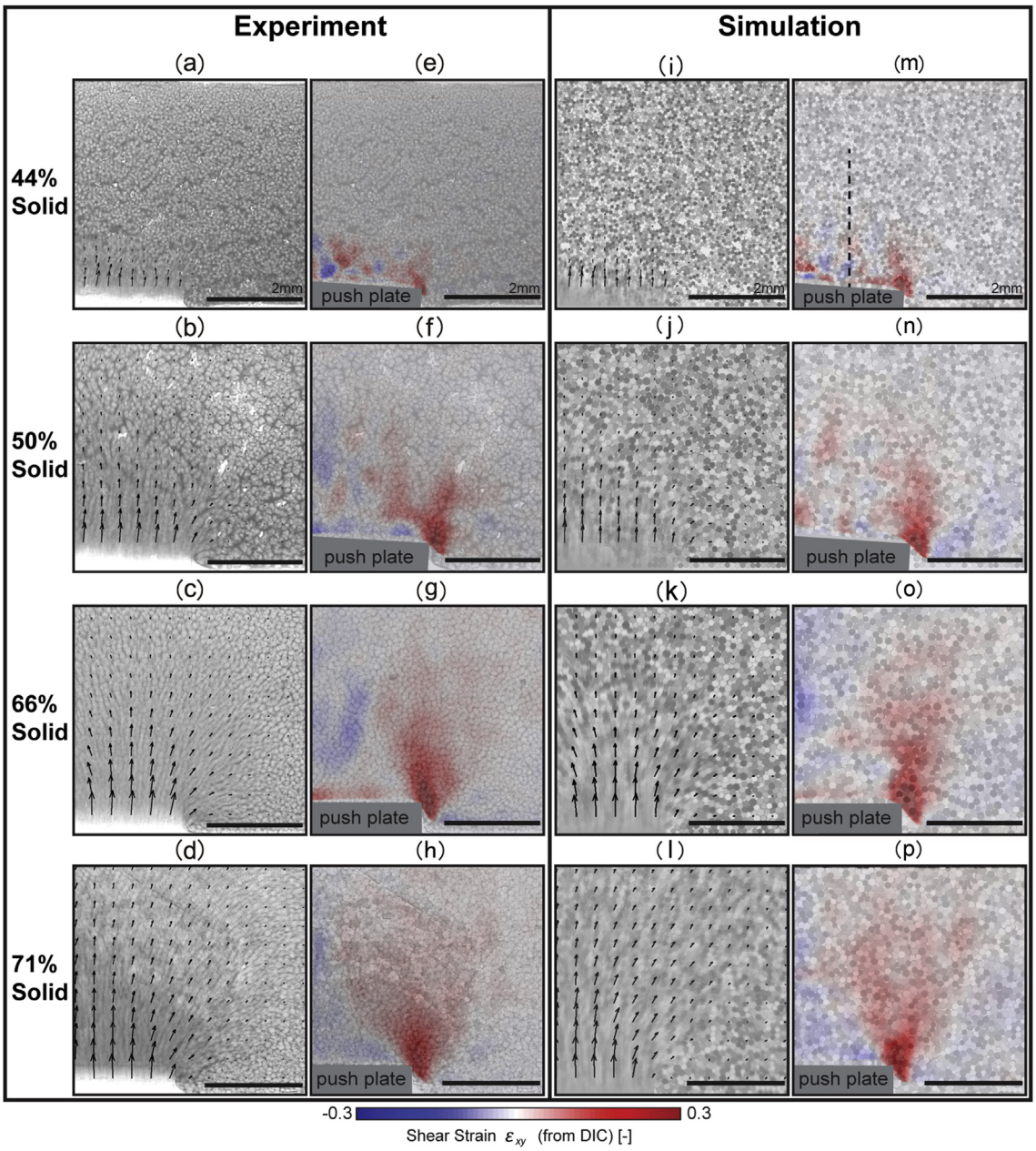

Fig. 5. (a–d) The superimposition of time-averaged raw images and displacement vectors for experiments. Each time-averaged image is the averaging of radiographic image sequences from the onset of deformation to the deformed image after $5\overline{d}$ increment of push-plate displacement, and the displacement vectors are derived from digital image correlation (DIC). The spacing between two adjacent displacement vectors is equal to the DIC subset size of that dataset. (e–h) Shear strain ε_{xy} field for experiments derived from DIC. The background images were chosen as the push-plate displacement $= 5\overline{d}$ radiographs. (i–l) The superimposition of time-averaged speckled DEM grain plots and displacement vectors. (m–p) Shear strain ε_{xy} field for simulations derived from DIC. The dashed line in (m) indicates the middle of the push-plate. The first row corresponds the 44% solid sample and simulation A, followed by 50% solid/simulation B, 66% solid/simulation C, and 71% solid/simulation D. Black-line scale bars read 2mm.

transitions of contraction-to-dilation response ahead of the push plate. The strain profiles acquired from triangulation are "jumpy" because the strains are calculated from the relative position changes of groups of three adjacent grains without any averaging by a REV.

It can be seen in Figs. 7–10 that, in general, there is good agreement between experiments and simulations. Specifically, the strain profiles from the 44% solid fraction experiment and simulation A (Fig. 7) show net-contraction in front of the push plate from the ε^n_{vol} profile in X-ray intensity processing on the experiment and divergence $(\varepsilon_{xx} + \varepsilon_{yy})$ profiles by DIC and triangulation on simulation A in Fig. 7c and e, and the distinctively negative (< -0.1) volumetric strain or divergence to $y \approx 12\overline{d}$ in the blue ROI (Fig. 7e) and at $x < 0$ in the red ROI (Fig. 7c) is captured well. The average shear strain profiles show minimal strain localisation in both the experiment and simulation (Fig. 7e and f).

For deformation at a slightly higher initial solid fraction (50% solid sample and simulation B) shown in Fig. 8, the volumetric strain ε^n_{vol} in the experiment and divergence profiles in the simulation are contractive in Fig. 8c and e, but less negative than in Fig. 7c and e. The shear strain profiles (Fig. 8d) go higher than in the 44% solid/simulation A of Fig. 7, indicating more strain-localisation

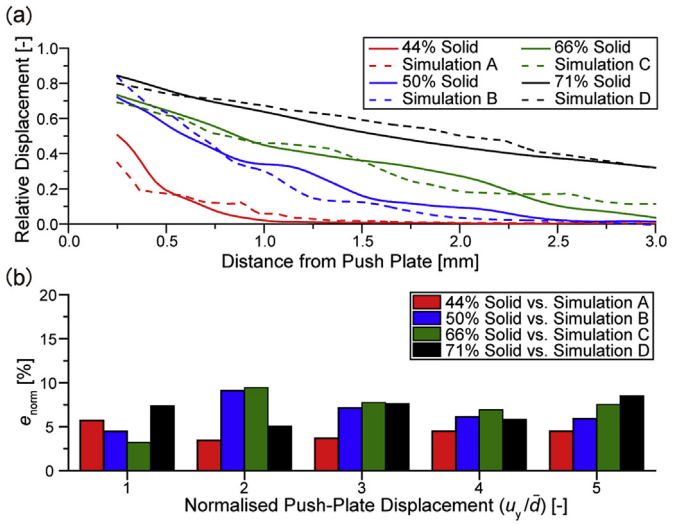

Fig. 6. (a) Line plot showing relative displacement (grain displacement magnitude divided by push-plate displacement) profiles of shear experiment and simulation deformation microstructures from a scan of displacement length field after $5\bar{d}$ increment of push-plate displacement. (b) Bar chart showing normalised error values e_{norm} (defined in Eq. (11)) with different push-plate displacement lengths for each dataset.

at higher solid fraction. Shear strain development occurs ahead of the push plate to $y \approx 15\bar{d}$ in both the experiment and corresponding simulation B, as shown in Fig. 8f.

Fig. 9 shows that deformation at higher initial solid fraction (66%) gives rise to localisation of both positive ε^n_{vol} and shear strain ε_{xy} in a similar location ($x \approx -5 \sim -3\bar{d}$ in the red ROI of Fig. 9c and d), which indicates a dilatant region [26]. The broad positive (dilative) ε^n_{vol} and divergence zone to $x \approx 12\bar{d}$ in Fig. 9c is a distinctive difference of strain response compared with the contractive low solid fraction datasets in Figs. 7c and 8c. In Fig. 9d, peaks of the shear strain profile are approximately located at the parting plane ($x \approx 0$). The co-location of the positive zone in divergence/volumetric strain profiles and ε_{xy} peaks in Fig. 9c and d gives a dilatant shear band width at 66% solid within the range $10\bar{d}$ to $15\bar{d}$, which is consistent with the measurements in past bulk rheology tests [9,17,95]. Analysis of the blue ROI, captures the contraction field immediately ahead of push-plate (Fig. 9e), followed by relatively smooth and positive profiles (normalised y axis from $2\bar{d}$ to $21\bar{d}$), in both the experiment and corresponding simulation C. The contraction field at the push plate front is due to local compaction at this location. Fig. 9c captures another negative (contractive) volumetric strain region to the far-right of the red ROI starting at $x = 12\bar{d}$, both in the ε^n_{vol} profile of the experiment and the divergence profiles from LBM-DEM simulation B, due to liquid drainage at this location (i.e. the suction of liquid from the far-right of the FOV to feed dilation near the parting-plane).

Fig. 10 is the response of the highest solid fraction dataset studied here (71%) which had the most net-dilative response and simulation D. Fig. 10c shows a liquid-enriched dilation zone at $x < 7\bar{d}$, followed by a contraction zone to the right of the red ROI (negative ε^n_{vol} or divergence at $x > 10\bar{d}$) both in the experiment and simulation D strain profiles. In the red ROI, both the experimental

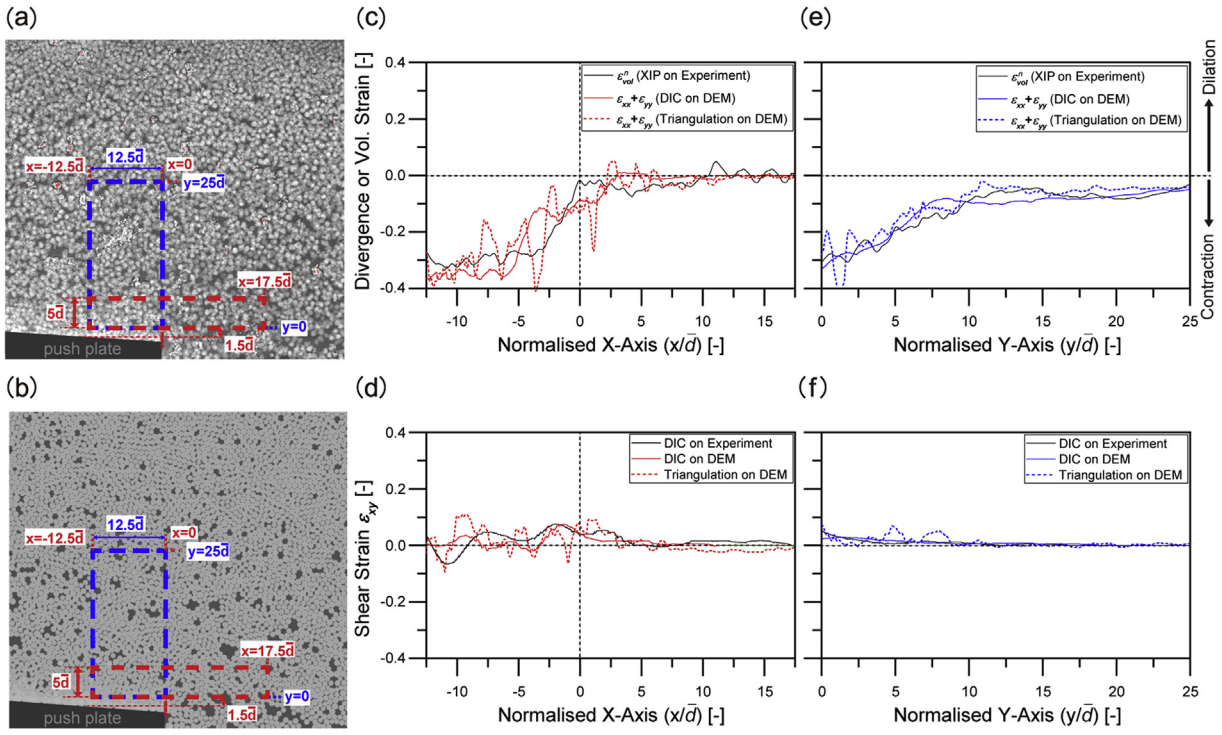

Fig. 7. Direct comparison among strain profiles from 44% solid sample and simulation A after $5\bar{d}$ increment of push-plate displacement. (a) Two regions of interest (ROIs) to study the profiles of strain. The first ROI outlined by the red-dashed line contains the region in front of push plate ($x < 0$), the parting plane ($x = 0$), and right-hand side of push plate ($x > 0$). The second ROI outlined by the blue-dashed line contains the region in front of the push plate ($y = 0$) to $y = 25\bar{d}$ (b) ROIs for the strain profile from simulation deformation microstructure in which the DEM grains were coloured semi-transparent light grey and the liquid domain were coloured dark grey. (c) The corresponding volumetric strain in (a) and divergence in (b) using the red ROI. The x-direction is scaled by the mean grain size $\bar{d}$ and the parting plane is set as the origin ($x = 0$). XIP = X-ray Intensity Processing. (d) The averaged shear strain profiles for the red ROI in (a) and (b). (e) The volumetric strain or divergence profiles for the blue ROI. The origin corresponds to the bottom edge of blue ROI. (f) The shear strain profiles for the blue ROI. (For interpretation of the references to colour in this figure legend, the reader is referred to the Web version of this article.)

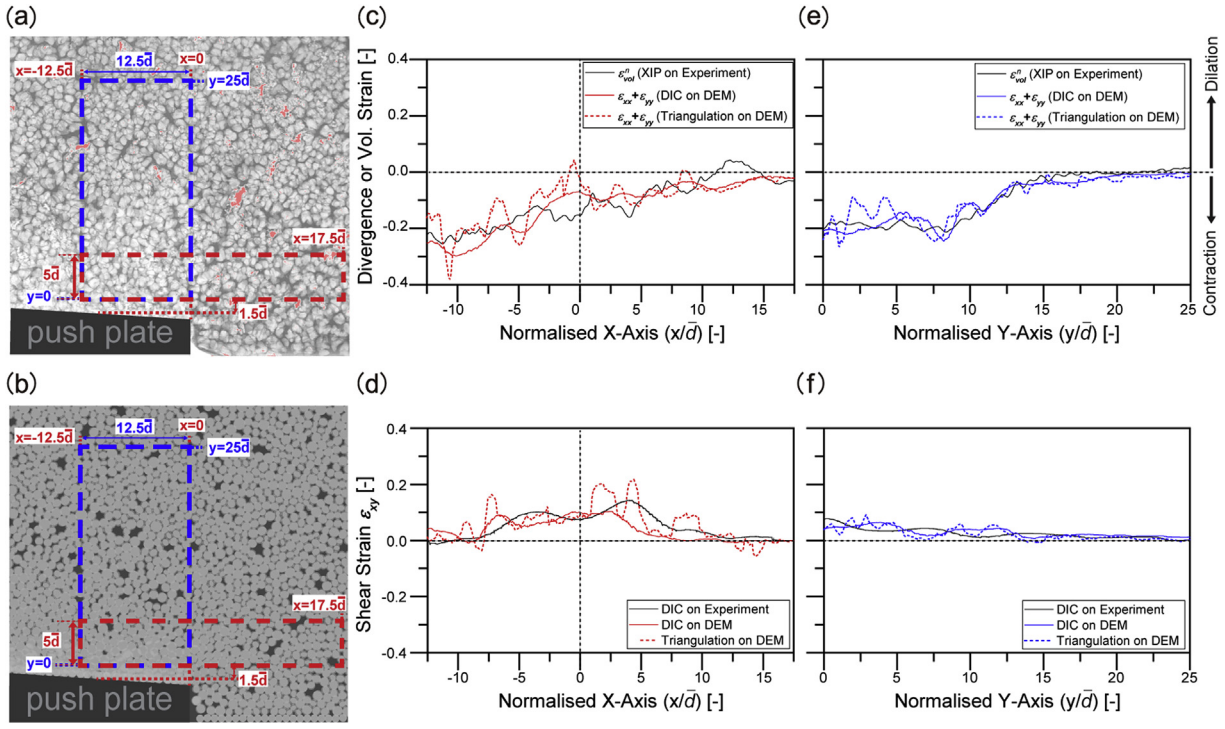

Fig. 8. Direct comparison among strain profiles from 50% solid sample and simulation B after 5$\bar{d}$ increment of push-plate displacement. (a) Two regions of interest (ROIs) to study the profiles of strain. (b) ROIs for the strain profile from the simulation deformation microstructure. (c) The corresponding volumetric strain in (a) and divergence in (b) using the red ROI. (d) The averaged shear strain profiles for red ROI in (a) and (b). (e) The volumetric strain or divergence profiles for the blue ROI. (f) The shear strain profiles for the blue ROI. (For interpretation of the references to colour in this figure legend, the reader is referred to the Web version of this article.)

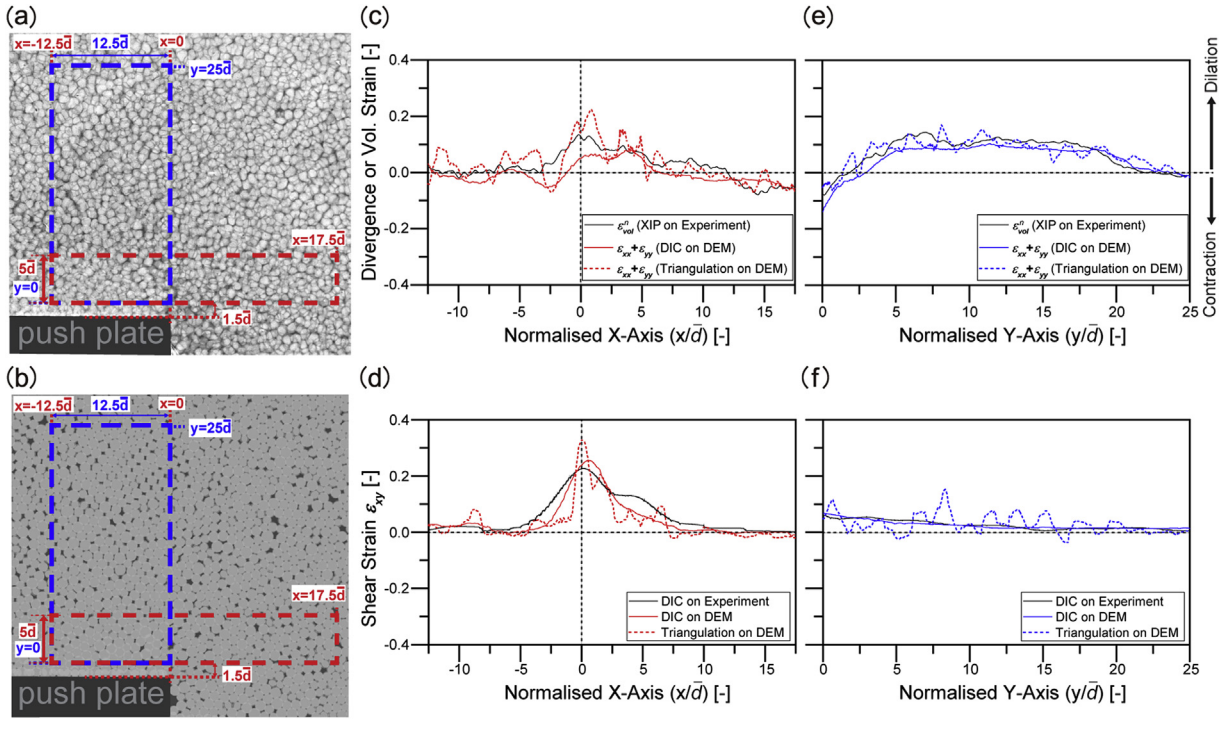

Fig. 9. Direct comparison among strain profiles from 66% solid sample and simulation C after 5$\bar{d}$ increment of push-plate displacement. (a) Two regions of interest (ROIs) to study the profiles of strain. (b) ROIs for the strain profile from the simulation deformation microstructure. (c) The corresponding volumetric strain in (a) and divergence in (b) using the red ROI. (d) The averaged shear strain profiles for the red ROI in (a) and (b). (e) The volumetric strain or divergence profiles for the blue ROI. (f) The shear strain profiles for the blue ROI. (For interpretation of the references to colour in this figure legend, the reader is referred to the Web version of this article.)

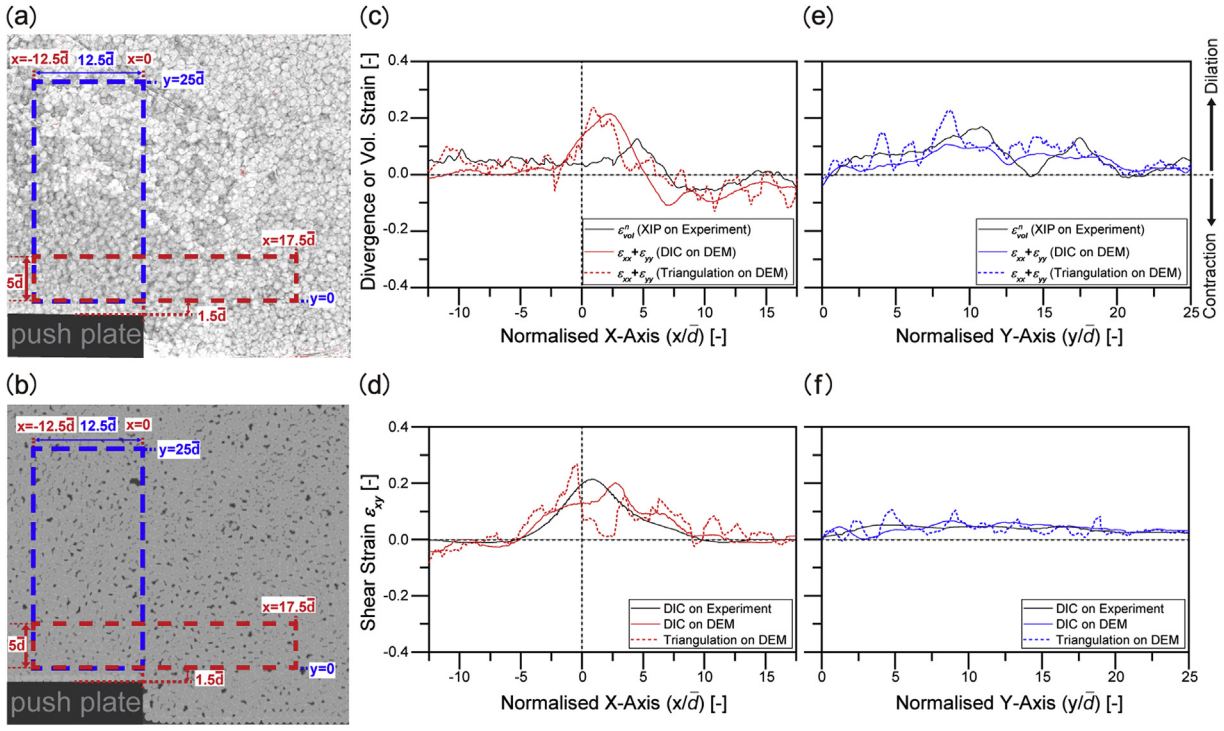

Fig. 10. Direct comparison among strain profiles from 71% solid sample and simulation D after $5\bar{d}$ increment of push-plate displacement. (a) Two regions of interest (ROIs) to study the profiles of strain. (b) ROIs for the strain profile from the simulation deformation microstructure. (c) The corresponding volumetric strain in (a) and divergence in (b) using the red ROI. (d) The averaged shear strain profiles for the red ROI in (a) and (b). (e) The volumetric strain or divergence profiles for the blue ROI. (f) The shear strain profiles for the blue ROI. (For interpretation of the references to colour in this figure legend, the reader is referred to the Web version of this article.)

ε^n_{vol} profile and simulated $\varepsilon_{xx}+\varepsilon_{yy}$ profile by triangulation show more positive dilative strains ahead of the push plate ($x<0\bar{d}$) than in Fig. 9c, but the peak width of the ε_{xy} profile in Fig. 10d is similar to Fig. 9d (from $10\bar{d}$ to $15\bar{d}$). The blue ROI contains a very small contractive region immediately ahead of the push plate, both in the 71% solid experiment and simulation D (Fig. 10e), and the ε^n_{vol} profile in the experiment then seems to have a periodic pattern with multiple peaks and valleys. The explanation of this phenomenon is incomplete liquid feeding during deformation at high solid fraction. As a result, the ε^n_{vol} field of the 71% solid sample (Fig. 3t) shows some island-like contractive areas where liquid is sucked to adjacent dilating zones. Those locally dilative zones correspond to peaks at $y\approx 10.5\bar{d}$ and $17.5\bar{d}$ in Fig. 10e. The complex heterogeneous liquid flow phenomena were not completely captured by the LBM-DEM simulation, but a reasonable correlation with experiment in Fig. 10e can still be observed.

While the simulations are 2D, the thin-sample experiments can be considered to be 2.5D with interactions from the confining walls. For the contractive region ahead of the push plate, the LBM-DEM simulation captures grain deformation by overlap between DEM grains which is tuned in the simple approach to plasticity in Fig. 2a to match the overlap in the through-thickness averaged radiographs. Therefore, although the 2D simulation model does not capture the change in thickness directly, it does capture the 'effective grain overlap' in regions of thickening due to compaction. For other regions, the change of sample thickness was low with overlap between grains of <0.1 $\bar{d}$ both in experiments and simulations, where the assumption of in-plane deformation is reasonable.

Comparison of all experimental and simulated profiles in Figs. 7–10 demonstrates that the coupled LBM-DEM simulations quantitatively captured many of the key features of the

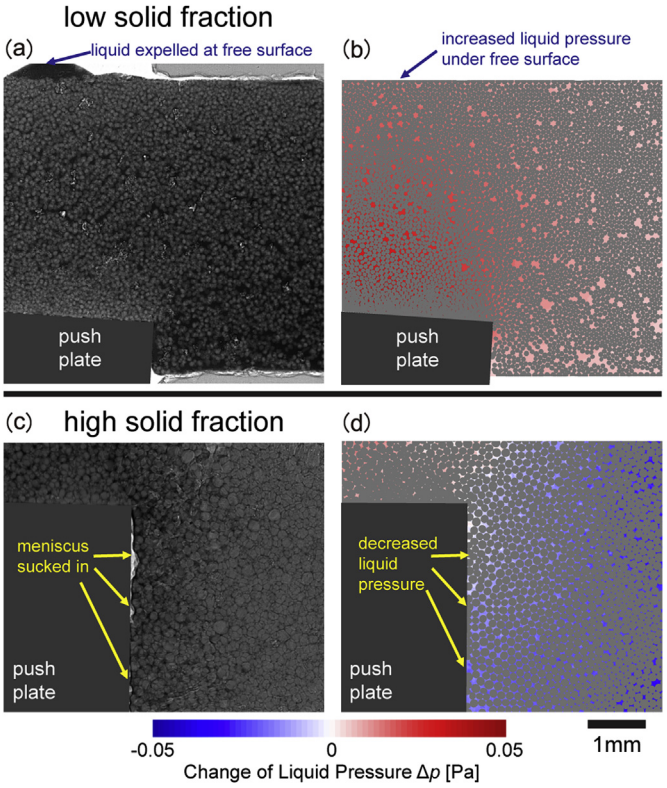

Fig. 11. Examples of the correlation between liquid behaviour in experiments and simulations. (a) Liquid expelled out at $\sim 11\bar{d}$ push-plate displacement in low solid fraction alloy (44%), (b) increased liquid pressure field in simulation A, (c) meniscus sucked in phenomenon at $\sim 28\bar{d}$ push-plate displacement in high solid fraction alloy, and (d) decreased liquid pressure field at the right edge of the push plate in simulation C.

heterogeneous volumetric and shear strain fields at solid fractions in the range 44–71 vol% solid, by only altering the initial packing fraction and initial average contact stress in the simulations. An important feature of the LBM-DEM simulations is that the local changes in packing density arise naturally as emergent phenomena. For example, in Fig. 4, Region B undergoes shear-induced dilation due to grains pushing each other apart in response to contact forces in both the experiment and simulation. The LBM-DEM simulations also reproduce further important phenomena observed in the experiments. For example, Fig. 11a shows that as the push plate continued to 11$\overline{d}$ displacement in the lowest solid fraction sample (44%), liquid was expelled from the sample-air interface at the top-left of the sample, indicating that an excess liquid pressure developed in this region. The simulated liquid pressure field in Fig. 11b correctly predicts a positive (red) change in liquid pressure in this region at 11$\overline{d}$ displacement and agrees with the location of the liquid expulsion. In Fig. 11b, note that the liquid pressure is highest on the lower-left-side of the Figure. However, the lower-left-side of the Figure is not a free surface; it is the edge of the experimental FOV. In SI Section 9, the full simulation domain is shown (which equals the whole experimental sample), where it can be seen that the true left-side free surface of the sample has a liquid pressure that is lower than the liquid pressure at the top of the FOV in Fig. 11b. It also shows that the region where liquid is expelled in Fig. 11a is the region with the highest liquid pressure near a surface in Fig. 11b.

On the other hand, Fig. 11c shows that, in the highest solid fraction sample, menisci are sucked in to the liquid at the free surface near the right edge of the push plate during deformation.

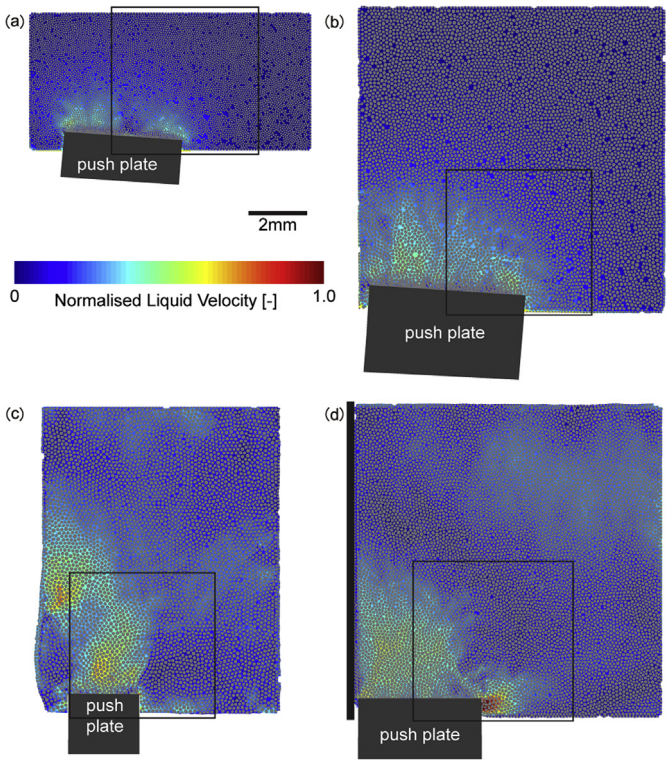

Fig. 12. Plots of liquid velocity magnitude field (normalised by push-plate velocity magnitude) surrounding grains for (a) simulation A (b) B, (c) C, and (d) D after 5$\overline{d}$ increment of push-plate displacement. The black solid-outline square indicates the corresponding FOV in radiography imaging in deformation experiments, and the radius of each grain is reduced by 80% of its original size to show the effect of hydrodynamic radius on the LBM liquid domain. The left-hand side wall installed in simulation D is consistent with the radiograph shown in Fig. SI-6d.

This is in agreement with the simulated liquid pressure field in Fig. 11d where a decreased liquid pressure (blue) region exists at this location. The different liquid pressure behaviour reflects the net-contractive response at low solid fraction (44%, Fig. 3q) and net-dilative shear response at high solid fraction (71%, Fig. 3t), and is a result of the coupling between local volumetric strains in the grain assembly and the liquid pressure field. This behaviour is expected to depend on the permeability and the strain rate and it was found that, when similar samples with initial solid fractions >73% were deformed, shear cracking occurred (not shown here).

The simulated push plate penetrates the compacted grain assembly in the DEM domain, and simultaneously acts as a moving solid boundary on the LBM liquid domain. Fig. 12 illustrates the simulated liquid flow field after a push plate displacement of 5$\overline{d}$. This field was constructed by colouring the LBM nodes by the relative velocity magnitude normalised by the push plate displacement rate. In Fig. 12, the localised high liquid flow rate in response to the penetration is very clear among all deformation datasets, but more prominent liquid flow across the whole sample in Figs. 12c and d is observed. The liquid flow is induced by the drag (momentum exchange) from adjacent DEM grains. Also in Fig. 12c and d, there is a subtle liquid flow towards the specimen centre from the membrane boundary with relative velocity magnitude <0.3. This can be related to a pressure differential that draws liquid to regions undergoing high shear-induced dilation. This is also seen in the experiments as a local contraction (grains moving closer together) to the right and bottom-right of Fig. 3s and t.

3.3. Stress-deformation response

A well-calibrated set of LBM-DEM simulation results can offer extra information that is not available in X-ray imaging. Fig. 13a is the evolution of normal push-plate stress tracked to 10$\overline{d}$ push-plate displacement, using the sum of grain-plate normal contact forces divided by the length of the push plate front similar to reference [96]. The normal stress gradually increases in lower solid fraction simulations A and B, while a peak push-plate stress can be found at ~2$\overline{d}$ displacement for higher solid fraction simulation C, and at 3$\overline{d}$ displacement for the highest solid fraction simulation D. It is noted that the predicted push-plate stress evolution cannot be compared with deformation experiments since the friction between the push-plate and Al_2O_3 window compromises our ability to accurately measure the push-plate load. Still, both the trend of increased peak stress in higher solid fraction simulations and the strain softening phenomenon observed in simulation C and D are consistent with previous deformation tests on granular/particulate materials including semi-solid alloys [10,19,31,97], experimental soils [96,98,99], and DEM-simulated granular soils [100,101]. Fig. 13b shows the evolution of total volumetric strain, which was calculated from:

$$\varepsilon_{vol}^{\mathrm{DEM}} = \ln\left(\frac{A_{def}}{A}\right) \tag{12}$$

where $\varepsilon_{vol}^{\mathrm{DEM}}$ is the volumetric strain directly evaluated from the change of area in the simulation samples, A and A_{def} are the area of the initial and deformed sample, which were obtained from the area of the polygon that joins the centroids of all surface bonding grains minus the push-plate penetration area. Fig. 13b clearly shows the transition from net-contractive simulation sets A and B with low initial solid fraction, to net-dilative simulation sets C and D with higher initial solid fraction. The reduction of sample area in A and B occurs because the initially loosely packed solid network in a low-solid fraction LBM-DEM simulation is prone to develop a

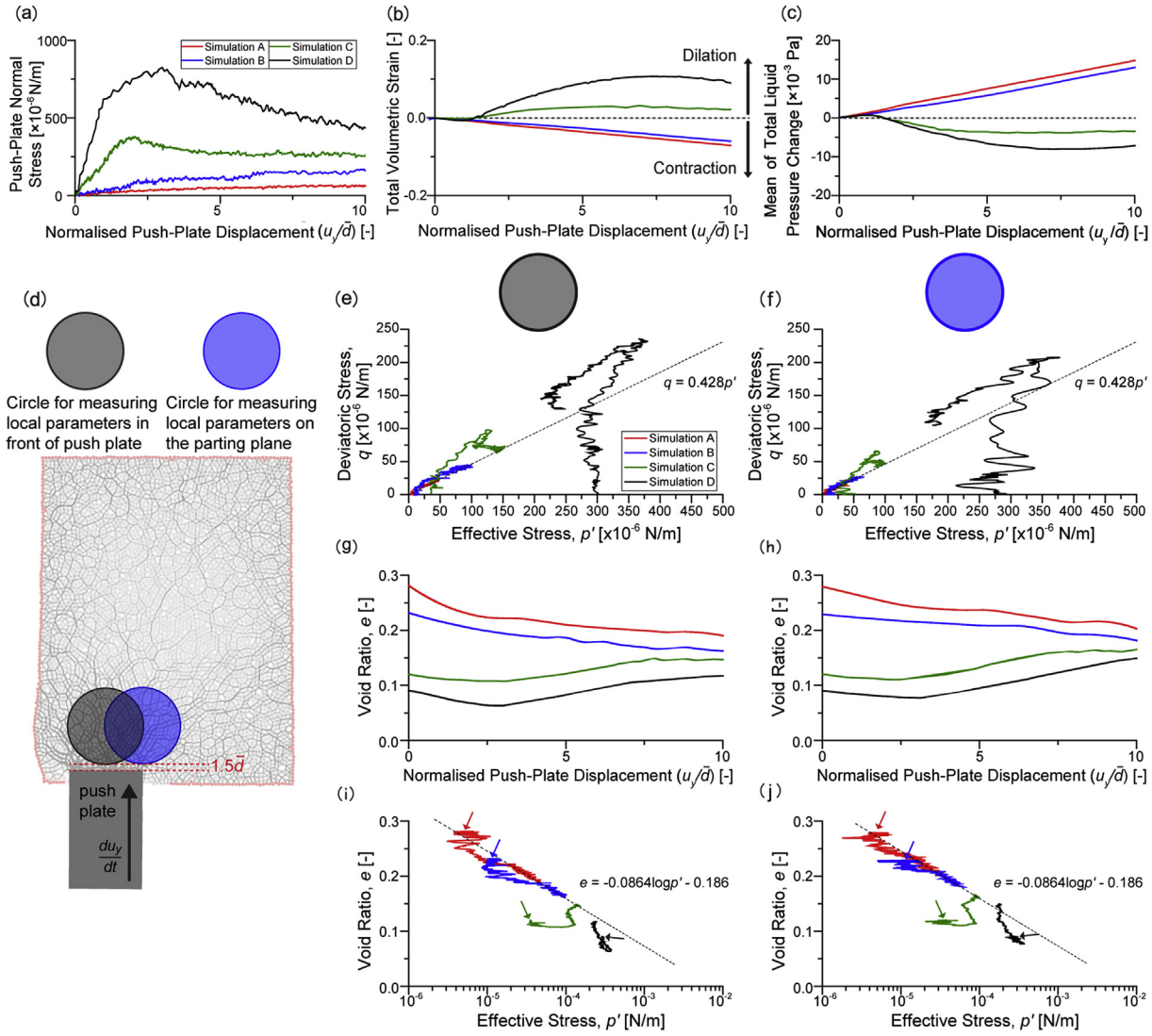

Fig. 13. (a) Evolution of normal push-plate stress, (b) volumetric strain ε'_{vol}, and (c) the mean of total liquid pressure change versus $10\bar{d}$ push-plate displacement. (d) Schematic illustration of the measurement regions for deriving local parameters. Diameter of measurement circles is $20\bar{d}$ in order to obtain representative stresses, and there is a $1.5\bar{d}$ gap between measurement circles and the push plate front. The horizontal position of the grey circle is in the middle of push plate, and the horizontal position of the blue circle is at the top-right corner of the push plate. The corresponding (e-f) $q - p\prime$, (g–h) $e - u_y/\bar{d}$, and (i–j) $e - \log p\prime$ plots are shown for black and blue measurement circles. Arrows in (i–j) indicate the initial state for each simulation. (For interpretation of the references to colour in this figure legend, the reader is referred to the Web version of this article.)

highly localised contractive field, resulting in the closure of liquid interstices. Simulation C, on the contrary, deforms with slightly net positive ε_{vol}^{DEM} behaviour because the contact force can be transmitted to the membrane to push the boundary outward and compensate for the local contractive response ahead of the push plate. Moreover, deformation in simulation D causes many of the liquid interstices to expand during grain rearrangement outside of the local compacted zone as well as the increased ability to push the enclosing membrane away, resulting in the net dilative deformation behaviour. Fig. 13b also shows the slight decrease of ε_{vol}^{DEM} after $6\bar{d}$ penetration on simulation C and $7.5\bar{d}$ penetration on simulation D. This is because the total solid fraction of the samples is decreased during net dilation, which increases the compressibility of the whole assembly.

The complex liquid behaviour at the free surface of semi-solid samples in the experiments can be related to the localised liquid pressure change Δp as shown in Fig. 11. We can then investigate the relationship between the change of volume of liquid-saturated samples and the overall liquid pressure changes. To get a representative trend, the mean liquid pressure change $\overline{\Delta p}$ was derived across the whole DEM assembly:

$$\overline{\Delta p} = \overline{\Delta p}(t) = \frac{\sum_{i=1}^{N_{node}} \Delta p(\mathbf{x}_i, t)}{N_{node}} \tag{13}$$

where N_{node} is the number of LBM nodes inside the DEM assembly. Fig. 13c is the evolution of $\overline{\Delta p}$ for each simulation set and comparison with Fig. 13b shows the interplay between the global liquid pressure change and the volumetric strain, The net-contractive simulations A and B have a net increase of liquid pressure in response to net contraction. The high solid fraction simulations C and D have a slightly positive pressure change up to $1.5\bar{d}$ deformation, followed by a decrease in liquid pressure in response to the global dilation, and the liquid pressure is near-constant once the peak dilatational volumetric strain is reached (Fig. 13b).

It is useful to investigate the local stress evolution in a circular

RV by explicit tracking of contact force vectors in the DEM system especially for the region in front of the push plate and the parting plane. Fig. 13d illustrates the setting of measurement circles in the DEM system to derive the local parameters such as the effective mean stress p', deviatoric stress q, and void ratio e. In two-dimensional DEM, the relationship between void ratio e and grain packing fraction (i.e. solid fraction) $f_{S.pk}$ is $e = (1 - f_{S.pk})/f_{S.pk}$. These local parameters were tracked to examine whether the DEM system behaves as a granular material such as a sand [22]. The diameter of the measurement region was chosen to be $20\overline{d}$ and includes ~250 grains; this is sufficiently large to obtain the effectively averaged behaviour of the regions of interest. Fig. 13e and f illustrate the evolution of the q versus p' relationship to $10\overline{d}$ displacement. Before shear deformation, the effective stress p' reflects the required mean stress on the DEM assembly to reach the desired packing fraction, and the mean stress values are similar between black and blue circles for every simulation set. The q- p' curves all start from $q = 0$ and the stresses are increasing for simulation A and B. It is noted that the low solid fraction simulation sets (red and blue in Fig. 13e and f) soon have an approximately constant q/p' ratio and follow the regression line $q = 0.428p'$, which can be related to the well-defined critical state in soil mechanics [22] stating that a frictional fluid should reach a macroscopic frictional constant $M = q/p'$. In contrast, the maximum deviatoric stress occurs in simulations C and D at 0.98×10^{-4} N/m and 2.35×10^{-4} N/m for the black circle, and 0.64×10^{-4} N/m and 2.07×10^{-4} N/m in the blue circle, respectively. After reaching the maximum deviatoric stress, both p' and q stresses decrease. The simulation C then reaches the $q = 0.428p'$ regression line, while the q- p' curves in simulation D show a nearly −50% decrease of stresses from the peak deviatoric stress point and moves towards the regression line (but does not reach it by $10\overline{d}$ push-plate displacement).

The evolution of void ratio is shown in Fig. 13g and h. The high contraction field in front of the push plate developed at an early stage of deformation ($3\overline{d}$) reduces the void ratio by about −0.03 in the black circle and about −0.01 in the blue circle. The void ratio decrease corresponds to the increase of local mean effective stresses as shown in Fig. 13i and j. There is a log-linear relationship between the final void ratio and the final value of p'; this corresponds to the critical state line concept accepted for granular soil behaviour [22]). The increase of void ratio in high solid fraction deformation is due to shear-induced dilation in both the black and blue circles.

Whilst this research used globular grains to prevent significant shape change during isothermal experiments and enable an efficient model, casting processes often create more complex morphologies such as equiaxed dendrites. Experiments [102] and DEM studies [64] have shown that dendrites form a solid network at lower solid fraction than globular grains due to the high liquid fraction within dendrite envelopes and due to the more complex shape of the envelopes. These factors will also alter the permeability [103], give more contacts per grain, and affect the local stresses acting on dendrites [64]. Future research can extend the LBM-DEM approach to dendritic microstructures in the future.

4. Conclusions

Time-resolved synchrotron X-ray radiography and coupled LBM-DEM simulations have been applied to investigate shear deformation mechanisms in equiaxed globular Al–Cu alloys at 44–71% solid. Microstructural and macroscopic responses to load have been quantified by intensity processing and digital image correlation (DIC) for radiographic imaging with >1000 grains in the field of view (FOV), and also reproduced by LBM-DEM after finding a single set of DEM parameters calibrated across all deformation experiments from 44 to 71% solid. From the results obtained by the various analysis approaches, the following conclusions can be drawn:

- The volumetric strain during semi-solid deformation due to local changes of solid fraction is strongly influenced by the initial solid fraction. A contractive strain field developed in shear or compressive deformation in alloys initially containing 44% and 50% solid. In contrast, significant net-dilation occurred during shear on the 66% and 71% solid samples.
- The mechanism of solid fraction increase during deformation is grains being pushed together by compaction, or by the liquid being sucked away. The solid fraction decrease, on the other hand, is due to shear-induced dilation by grains pushing one another apart during grain rearrangement in a solid network, similar to phenomena in compacted granular/particulate materials.
- Deformation was highly heterogeneous and the strain was strongly localised. Both the experiments and simulations agree with the trend of net-contraction ahead of the push plate and, in high solid fraction deformation, the co-location of dilative volumetric strain and shear strain in a region with width of 10–15 mean grains wide. Additionally, a contraction field formed outside the locally dilating regions in high solid fraction samples due to liquid being sucked away to feed dilation.
- The coupled LBM-DEM model naturally simulates the change of packing density in primary Al grains as an emergent phenomenon, and captures the complex liquid behaviour recorded in radiographs from the simulated liquid pressure change.
- The calibrated LBM-DEM model provided information on both the local stresses and void ratios; these data show that the material exhibits a load deformation response that can be described by the critical state framework for soil behaviour.

Acknowledgements

The in-situ observations were supported by a Grant-in-Aid for Scientific Research (S) (No. 17H06155). Experiments were conducted at the SPring-8 Synchrotron on BL20B2 under Proposal No. 2015A1318 and 2017B1523. Analysis was carried out under the EPSRC Grant EP/K026763/1. T.C. Su gratefully acknowledges a President's scholarship from Imperial College London.

Appendix A. Supplementary data

Supplementary data to this article can be found online at https://doi.org/10.1016/j.actamat.2018.10.006.

References

[1] A. Kaye, A. Street, Die Casting Metallurgy, Butterworth Scientific, London, 1982.
[2] E.J. Vinarcik, High Integrity Die Casting Processes, John Wiley & Sons, New Jersey, 2002.
[3] W. Andresen, Die Cast Engineering: a Hydraulic, Thermal, and Mechanical Process, CRC Press, New York, 2004.
[4] X.S. Huang, L.J. He, G.B. Mi, P.J. Li, Characteristics of defect bands and their formation mechanisms in A356 wheel fabricated by horizontal squeeze casting, Mater. Sci. Technol. 31 (4) (2015) 400–408.
[5] M. Masoumi, H. Hu, Influence of applied pressure on microstructure and tensile properties of squeeze cast magnesium Mg-Al-Ca alloy, Mater. Sci. Eng., A 528 (10–11) (2011) 3589–3593.
[6] R. Cook, P.G. Grocock, P.M. Thomas, D.V. Edmonds, J.D. Hunt, Development of the twin-roll casting process, J. Mater. Process. Technol. 55 (2) (1995) 76–84.
[7] C. Gras, M. Meredith, J.D. Hunt, Microdefects formation during the twin-roll

casting of Al-Mg-Mn aluminium alloys, J. Mater. Process. Technol. 167 (1) (2005) 62–72.
[8] Z. Bian, I. Bayandorian, H.W. Zhang, G. Scamans, Z. Fan, Extremely fine and uniform microstructure of magnesium AZ91D alloy sheets produced by melt conditioned twin roll casting, Mater. Sci. Technol. 25 (5) (2009) 599–606.
[9] C.M. Gourlay, A.K. Dahle, Dilatant shear bands in solidifying metals, Nature 445 (7123) (2007) 70–73.
[10] C.M. Gourlay, B. Meylan, A.K. Dahle, Shear mechanisms at 0-50% solid during equiaxed dendritic solidification of an AZ91 magnesium alloy, Acta Mater. 56 (14) (2008) 3403–3413.
[11] C.M. Gourlay, H.I. Laukli, A.K. Dahle, Defect band characteristics in Mg-Al and Al-Si high-pressure die castings, Metall. Mater. Trans. 38A (8) (2007) 1833–1844.
[12] S. Otarawanna, C.M. Gourlay, H.I. Laukli, A.K. Dahle, The thickness of defect bands in high-pressure die castings, Mater. Char. 60 (12) (2009) 1432–1441.
[13] M.C. Flemings, Solidification Processing, McGraw-Hill, New York, 1974.
[14] C.P. Chen, C.Y.A. Tsao, Semi-solid deformation of non-dendritic structures. 1. Phenomenological behavior, Acta Mater. 45 (5) (1997) 1955–1968.
[15] S. Otarawanna, H.I. Laukli, C.M. Gourlay, A.K. Dahle, Feeding mechanisms in high-pressure die castings, Metall. Mater. Trans. 41a (7) (2010) 1836–1846.
[16] M.S. Kim, S.H. Kim, H.W. Kim, Deformation-induced center segregation in twin-roll cast high-Mg Al–Mg strips, Scripta Mater. 152 (2018) 69–73.
[17] B. Meylan, S. Terzi, C.M. Gourlay, A.K. Dahle, Dilatancy and rheology at 0-60% solid during equiaxed solidification, Acta Mater. 59 (8) (2011) 3091–3101.
[18] E. Tzimas, A. Zavaliangos, Mechanical behavior of alloys with equiaxed microstructure in the semisolid state at high solid content, Acta Mater. 47 (2) (1999) 517–528.
[19] T. Sumitomo, D.H. StJohn, T. Steinberg, The shear behaviour of partially solidified Al-Si-Cu alloys, Mater. Sci. Eng., A 289 (1–2) (2000) 18–29.
[20] O. Reynolds, LVII. On the dilatancy of media composed of rigid particles in contact. With experimental illustrations, Philos. Mag. Series 5 20 (127) (1885) 469–481.
[21] W. Powrie, Soil Mechanics: Concepts and Applications, second ed., Taylor & Francis, New York, 2004.
[22] A. Schofield, P. Wroth, Critical State Soil Mechanics, McGraw-Hill, New York, 1968.
[23] C.M. Gourlay, A.K. Dahle, T. Nagira, N. Nakatsuka, K. Nogita, K. Uesugi, H. Yasuda, Granular deformation mechanisms in semi-solid alloys, Acta Mater. 59 (12) (2011) 4933–4943.
[24] C.M. Gourlay, C. O'Sullivan, J. Fonseca, L. Yuan, K.M. Kareh, T. Nagira, H. Yasuda, Synchrotron radiography studies of shear-induced dilation in semisolid Al alloys and steels, JOM 66 (8) (2014) 1415–1424.
[25] T. Nagira, C.M. Gourlay, A. Sugiyama, M. Uesugi, Y. Kanzawa, M. Yoshiya, K. Uesugi, K. Umetani, H. Yasuda, Direct observation of deformation in semi-solid carbon steel, Scripta Mater. 64 (12) (2011) 1129–1132.
[26] T. Nagira, H. Yokota, S. Morita, H. Yasuda, M. Yoshiya, C.M. Gourlay, A. Sugiyama, K. Uesugi, K. Umetani, Characterization of shear deformation based on in-situ observation of deformation in semi-solid Al-Cu alloys and water-particle mixture, ISIJ Int. 53 (7) (2013) 1195–1201.
[27] J. Fonseca, C. O'Sullivan, T. Nagira, H. Yasuda, C.M. Gourlay, In situ study of granular micromechanics in semi-solid carbon steels, Acta Mater. 61 (11) (2013) 4169–4179.
[28] T. Nagira, S. Morita, H. Yokota, H. Yasuda, C.M. Gourlay, M. Yoshiya, A. Sugiyama, K. Uesugi, A. Takeuchi, Y. Suzuki, In situ observation of deformation in semi-solid Fe-C alloys at high shear rate, Metall. Mater. Trans. 45A (12) (2014) 5613–5623.
[29] S. Zabler, A. Rack, A. Rueda, L. Helfen, F. Garcia-Moreno, J. Banhart, Direct observation of particle flow in semi-solid alloys by synchrotron X-ray microradioscopy, Phys. Status Solidi 207 (3) (2010) 718–723.
[30] S. Zabler, A. Ershov, A. Rack, F. Garcia-Moreno, T. Baumbach, J. Banhart, Particle and liquid motion in semi-solid aluminium alloys: a quantitative in situ microradioscopy study, Acta Mater. 61 (4) (2013) 1244–1253.
[31] K.M. Kareh, P.D. Lee, R.C. Atwood, T. Connolley, C.M. Gourlay, Revealing the micromechanisms behind semi-solid metal deformation with time-resolved X-ray tomography, Nat. Commun. 5 (2014) 1–7.
[32] B. Cai, P.D. Lee, S. Karagadde, T.J. Marrow, T. Connolley, Time-resolved synchrotron tomographic quantification of deformation during indentation of an equiaxed semi-solid granular alloy, Acta Mater. 105 (2016) 338–346.
[33] S. Terzi, L. Salvo, M. Suery, N. Limodin, J. Adrien, E. Maire, Y. Pannier, M. Bornert, D. Bernard, M. Felberbaum, M. Rappaz, E. Bollerr, In situ X-ray tomography observation of inhomogeneous deformation in semi-solid aluminium alloys, Scripta Mater. 61 (5) (2009) 449–452.
[34] K.M. Kareh, C. O'Sullivan, T. Nagira, H. Yasuda, C.M. Gourlay, Dilatancy in semi-solid steels at high solid fraction, Acta Mater. 125 (2017) 187–195.
[35] A. Zavaliangos, Modeling of the mechanical behavior of semisolid metallic alloys at high volume fractions of solid, Int. J. Mech. Sci. 40 (10) (1998) 1029–1041.
[36] J.J. Wang, A.B. Phillion, G.M. Lu, Development of a visco-plastic constitutive modeling for thixoforming of AA6061 in semi-solid state, J. Alloy. Comp. 609 (2014) 290–295.
[37] X. Hu, Q. Zhu, H. Atkinson, H. Lu, F. Zhang, H. Dong, Y. Kang, A time-dependent power law viscosity model and its application in modelling semi-solid die casting of 319s alloy, Acta Mater. 124 (2017) 410–420.
[38] M.H. Sheikh-Ansari, M. Aghaie-Khafri, Shear localization in semi-solid deformation: a bifurcation theory approach, Mech. Res. Commun. 89 (2018) 1–5.
[39] M.S. Ansari, M. Aghaie-Khafri, Predicting flow localization in semi-solid deformation, Int. J. Material Form. 11 (2) (2018) 165–173.
[40] O. Ludwig, J.M. Drezet, C.L. Martin, M. Suery, Rheological behavior of Al-Cu alloys during solidification: constitutive modeling, experimental identification, and numerical study, Metall. Mater. Trans. 36a (6) (2005) 1525–1535.
[41] O. Ludwig, J.M. Drezet, P. Meneses, C.L. Martin, M. Suery, Rheological behavior of a commercial AA5182 aluminum alloy during solidification, Mater. Sci. Eng., A 413 (2005) 174–179.
[42] T. Koshikawa, M. Bellet, C.A. Gandin, H. Yamamura, M. Bobadilla, Experimental study and two-phase numerical modeling of macrosegregation induced by solid deformation during punch pressing of solidifying steel ingots, Acta Mater. 124 (2017) 513–527.
[43] T. Kajitani, J.M. Drezet, M. Rappaz, Numerical simulation of deformation-induced segregation in continuous casting of steel, Metall. Mater. Trans. 32 (6) (2001) 1479–1491.
[44] C.S. Li, B.G. Thomas, Thermomechanical finite-element model of shell behavior in continuous casting of steel, Metall. Mater. Trans. B 35 (6) (2004) 1151–1172.
[45] J. Domitner, M.H. Wu, A. Kharicha, A. Ludwig, B. Kaufmann, J. Reiter, T. Schaden, Modeling the effects of strand surface bulging and mechanical soft reduction on the macrosegregation formation in steel continuous casting, Metall. Mater. Trans. 45a (3) (2014) 1415–1434.
[46] A.B. Phillion, S.L. Cockcroft, P.D. Lee, A three-phase simulation of the effect of microstructural features on semi-solid tensile deformation, Acta Mater. 56 (16) (2008) 4328–4338.
[47] M. M'Hamdi, A. Mo, H.G. Fjaer, TearSim: a two-phase model addressing hot tearing formation during aluminum direct chill casting, Metall. Mater. Trans. 37a (10) (2006) 3069–3083.
[48] S. Vernede, J.A. Dantzig, M. Rappaz, A mesoscale granular model for the mechanical behavior of alloys during solidification, Acta Mater. 57 (5) (2009) 1554–1569.
[49] C. O'Sullivan, Particulate Discrete Element Modelling: a Geomechanics Perspective, Spon, London, 2011.
[50] H. Shimizu, S. Murata, T. Ishida, The distinct element analysis for hydraulic fracturing in hard rock considering fluid viscosity and particle size distribution, Int. J Rock. Mech. Min. 48 (5) (2011) 712–727.
[51] D.F. Boutt, B.K. Cook, B.J.O.L. McPherson, J.R. Williams, Direct simulation of fluid-solid mechanics in porous media using the discrete element and lattice-Boltzmann methods, J. Geophys. Res.-Sol. Ea. 112 (B10) (2007).
[52] G.W. Bergantz, J.M. Schleicher, A. Burgisser, Open-system dynamics and mixing in magma mushes, Nat. Geosci. 8 (10) (2015) 793–796.
[53] A. Leonardi, F.K. Wittel, M. Mendoza, H.J. Herrmann, Coupled DEM-LBM method for the free-surface simulation of heterogeneous suspensions, Comput. Part. Mech. 1 (1) (2014) 3–13.
[54] V. Slowik, J.W. Ju, Discrete modeling of plastic cement paste subjected to drying, Cement Concr. Compos. 33 (9) (2011) 925–935.
[55] C.L. Martin, D. Bouvard, S. Shima, Study of particle rearrangement during powder compaction by the discrete element method, J. Mech. Phys. Solid. 51 (4) (2003) 667–693.
[56] H.P. Zhu, Z.Y. Zhou, R.Y. Yang, A.B. Yu, Discrete particle simulation of particulate systems: a review of major applications and findings, Chem. Eng. Sci. 63 (23) (2008) 5728–5770.
[57] B.K. Cook, D.R. Noble, J.R. Williams, A direct simulation method for particle-fluid systems, Eng. Comput. 21 (2–4) (2004) 151–168.
[58] D. Noble, J. Torczynski, A lattice-Boltzmann method for partially saturated computational cells, Int. J. Mod. Phys. C 9 (08) (1998) 1189–1201.
[59] Y.H. Han, P.A. Cundall, Resolution sensitivity of momentum-exchange and immersed boundary methods for solid-fluid interaction in the lattice Boltzmann method, Int. J. Numer. Methods Fluid. 67 (3) (2011) 314–327.
[60] Y.H. Han, P.A. Cundall, LBM-DEM modeling of fluid-solid interaction in porous media, Int. J. Numer. Anal. Model. 37 (10) (2013) 1391–1407.
[61] D.H. Johnson, F. Vahedifard, B. Jelinek, J.F. Peters, Micromechanics of undrained response of dilative granular media using a coupled DEM-LBM model: a case of biaxial test, Comput. Geotech. 89 (2017) 103–112.
[62] M. Sistaninia, A.B. Phillion, J.M. Drezet, M. Rappaz, Simulation of semi-solid material mechanical behavior using a combined discrete/finite element method, Metall. Mater. Trans. 42A (1) (2011) 239–248.
[63] M. Sistaninia, S. Terzi, A.B. Phillion, J.M. Drezet, M. Rappaz, 3-D granular modeling and in situ X-ray tomographic imaging: a comparative study of hot tearing formation and semi-solid deformation in Al-Cu alloys, Acta Mater. 61 (10) (2013) 3831–3841.
[64] L. Yuan, C. O'Sullivan, C.M. Gourlay, Exploring dendrite coherency with the discrete element method, Acta Mater. 60 (3) (2012) 1334–1345.
[65] K. Umetani, K. Uesugi, M. Kobatake, A. Yamamoto, T. Yamashita, S. Imai, Synchrotron radiation microimaging in rabbit models of cancer for preclinical testing, Nucl. Instrum. Methods Phys. Res. 609 (1) (2009) 38–49.
[66] D. Swinehart, The Beer-Lambert law, J. Chem. Educ. 39 (7) (1962) 333.
[67] S.R. Sternberg, Biomedical image-processing, Computer 16 (1) (1983) 22–34.
[68] H. Yasuda, T. Nagira, M. Yoshiya, N. Nakatsuka, A. Sugiyama, K. Uesugi, K. Umetani, Development of X-ray imaging for observing solidification of carbon steels, ISIJ Int. 51 (3) (2011) 402–408.
[69] S. Ganesan, D.R. Poirier, Densities of aluminum-rich aluminum-copper alloys during solidification, Metall. Trans. A 18 (4) (1987) 721–723.
[70] J.L. Murray, The aluminium-copper system, Int. Met. Rev. 30 (1) (1985)

211–234.
[71] J.H. Hubbell, S.M. Seltzer, Tables of X-Ray Mass Attenuation Coefficients and Mass Energy-absorption Coefficients from 1 KeV to 20 MeV for Elements Z = 1 to 92 and 48 Additional Substances of Dosimetric Interest. Radiation Physics Division, PML, NIST, 1996.
[72] J.A. Dantzig, M. Rappaz, Solidification, EPFL Press, London, 2009.
[73] S. Ganesan, D.R. Poirier, Conservation of mass and momentum for the flow of interdendritic liquid during solidification, Metall. Trans. B 21 (1) (1990) 173–181.
[74] L.E. Malvern, Introduction to the Mechanics of a Continuous Medium, Prentice-Hall, Inc., Englewood Cliffs, New Jersey, 1969.
[75] M. Bornert, F. Bremand, P. Doumalin, J.C. Dupre, M. Fazzini, M. Grediac, F. Hild, S. Mistou, J. Molimard, J.J. Orteu, L. Robert, Y. Surrel, P. Vacher, B. Wattrisse, Assessment of digital image correlation measurement errors: methodology and results, Exp. Mech. 49 (3) (2009) 353–370.
[76] F.J. Yang, X.Y. He, C.G. Quan, Characterization of dynamic microgyroscopes by use of temporal digital image correlation, Appl. Opt. 45 (30) (2006) 7785–7790.
[77] M. Oda, H. Kazama, Microstructure of shear bands and its relation to the mechanisms of dilatancy and failure of dense granular soils, Geotechnique 48 (4) (1998) 465–481.
[78] Y.H. Wang, S.C. Leung, A particulate-scale investigation of cemented sand behavior, Can. Geotech. J. 45 (1) (2008) 29–44.
[79] S. Nemat-Nasser, Averaging theorems in finite deformation plasticity, Mech. Mater. 31 (8) (1999) 493–523.
[80] E. Masad, B. Muhunthan, Three-dimensional characterization and simulation of anisotropic soil fabric, J. Geotech. Geoenviron. 126 (3) (2000) 199–207.
[81] A. Drescher, G.D.J. De Jong, Photoelastic verification of a mechanical model for the flow of a granular material, J. Mech. Phys. Solid. 20 (5) (1972) 337–340.
[82] K. Iwashita, M. Oda, Rolling resistance at contacts in simulation of shear band development by DEM, J. Eng. Mech.-Asce 124 (3) (1998) 285–292.
[83] J.K. Morgan, M.S. Boettcher, Numerical simulations of granular shear zones using the distinct element method - 1. Shear zone kinematics and the micromechanics of localization, J. Geophys Res-Sol Ea 104 (B2) (1999) 2703–2719.
[84] M.J. Jiang, H.B. Yan, H.H. Zhu, S. Utili, Modeling shear behavior and strain localization in cemented sands by two-dimensional distinct element method analyses, Comput. Geotech. 38 (1) (2011) 14–29.
[85] A. Cottrell, R. Stokes, Effects of temperature on the plastic properties of aluminium crystals, in: Proceedings of the Royal Society of London A: Mathematical, Physical and Engineering Sciences, The Royal Society, 1955, pp. 17–34.
[86] J.J. Hu, J.Y. Zhang, Z.H. Jiang, X.D. Ding, Y.S. Zhang, S. Han, J. Sun, J.S. Lian, Plastic deformation behavior during unloading in compressive cyclic test of nanocrystalline copper, Mater. Sci. Eng., A 651 (2016) 999–1009.
[87] S. Ganesan, R. Speiser, D.R. Poirier, Viscosities of aluminum-rich Al–Cu liquid alloys, Metall. Trans. B 18 (2) (1987) 421–424.
[88] Y. Han, P. Cundall, Verification of two-dimensional LBM-DEM coupling approach and its application in modeling episodic sand production in borehole, Petroleum 3 (2) (2017) 179–189.
[89] K.K. Soundararajan, Multi-scale Multiphase Modelling of Granular Flows, PhD Thesis, University of Cambridge, 2015.
[90] K. Kumar, J.Y. Delenne, K. Soga, Mechanics of granular column collapse in fluid at varying slope angles, J. Hydrodyn. 29 (4) (2017) 529–541.
[91] X.Y. He, Q.S. Zou, L.S. Luo, M. Dembo, Analytic solutions of simple flows and analysis of nonslip boundary conditions for the lattice Boltzmann BGK model, J. Stat. Phys. 87 (1–2) (1997) 115–136.
[92] P. Lallemand, L.S. Luo, Lattice Boltzmann method for moving boundaries, J. Comput. Phys. 184 (2) (2003) 406–421.
[93] PFC-particle Flow Code 5.0, Itasca Consulting Group, Inc., Minneapolis, USA, 2014.
[94] D. Markauskas, R. Kacianauskas, Investigation of rice grain flow by multi-sphere particle model with rolling resistance, Granul. Matter 13 (2) (2011) 143–148.
[95] B. Meylan, S. Terzi, C.M. Gourlay, M. Suery, A.K. Dahle, Development of shear bands during deformation of partially solid alloys, Scripta Mater. 63 (12) (2010) 1185–1188.
[96] M.J. Jiang, H.S. Yu, D. Harris, Discrete element modelling of deep penetration in granular soils, Int. J. Numer. Anal. Model. 30 (4) (2006) 335–361.
[97] S.A. Metz, M.C. Flemings, Hot tearing in cast metals, AFS Trans 77 (1969) 329–334.
[98] X.S. Li, Y.F. Dafalias, Dilatancy for cohesionless soils, Geotechnique 50 (4) (2000) 449–460.
[99] L. Rothenburg, N.P. Kruyt, Critical state and evolution of coordination number in simulated granular materials, Int. J. Solid Struct. 41 (21) (2004) 5763–5774.
[100] S. Lobo-Guerrero, L.E. Vallejo, Discrete element method evaluation of granular crushing under direct shear test conditions, J. Geotech. Geoenviron. 131 (10) (2005) 1295–1300.
[101] S. Lobo-Guerrero, L.E. Vallejo, DEM analysis of crushing around driven piles in granular materials, Geotechnique 55 (8) (2005) 617–623.
[102] L. Arnberg, G. Chai, L. Backerud, Determination of dendritic coherency in solidifying melts by theological measurements, Mater. Sci. Eng., A 173 (1–2) (1993) 101–103.
[103] O. Nielsen, L. Arnberg, A. Mo, H. Thevik, Experimental determination of mushy zone permeability in aluminum-copper alloys with equiaxed microstructures, Metall. Mater. Trans. 30 (9) (1999) 2455–2462.